

A GONIOREFLECTOMETER FOR MEASURING THE
BIDIRECTIONAL REFLECTANCE OF MATERIAL FOR
USE IN ILLUMINATION COMPUTATION

A Thesis

Presented to the Faculty of the Graduate School

of Cornell University

in Partial Fulfillment of the Requirements for the Degree of

Master of Science

by

Sing Choong Foo

August 1997

© Sing Choong Foo 1997

ALL RIGHTS RESERVED

Abstract

This thesis presents the detailed design and measurement procedures of an automated three-axis gonireflectometer for measuring the bidirectional reflectance distribution function (BRDF) of an isotropic material for use in computer graphics rendering. The working gonireflectometer is a modification of a partially completed instrument donated by Kodak to the Light Measurement Laboratory of the Cornell Program of Computer Graphics.

The gonireflectometer consists of a broad band light source that emits parallel rays in the visible wavelength range. The light source revolves around the test sample which itself has two degrees of freedom of rotation. The detector is stationary and views the test sample via a folding mirror. The detector consists of external focusing optics, a diffraction grating spectrograph, and a diode-array sensor. The system has a high dynamic range and can measure the reflection at high grazing angles (up to 86°). Both absolute calibration by measuring the direct irradiance, and relative calibration by using a reference sample, can be used for converting measurements to BRDF values.

BRDFs of three different samples, a white PTFE sample (Spectralon), a latex blue paint, and a matte-finished steel plate (Q-Panel R-46), were measured with

the gonireflectometer. The results are presented along with close comparisons to data published by other facilities. Specular reflectance and directional-hemispherical reflectance measured with the instrument were cross-checked to measurements made with an Optronic Spectroradiometer (OL-750).

Biographical Sketch

Sing Choong Foo was born in Ipoh, Perak, Malaysia. After graduating from Poi Lam High School in Ipoh, Sing Choong came to Cornell University in 1989. Sing Choong completed a B.S. and an M.Eng in applied and engineering physics prior to enrolling in the computer graphics M.S. program. He managed the Light Measurement Laboratory in the Cornell Program of Computer Graphics from the summer of 1993 until May 1997.

To my parents.

Acknowledgements

First of all, I wish to thank Professor Donald Greenberg for granting me the opportunity to be part of the computer graphics program, and for his advice and support over the last four years. I am most grateful and indebted to Professor Ken Torrance, my thesis advisor who has supervised all the work I have done in the Light Measurement Lab, and who has not only taught me science, but tried very hard to teach me work discipline. Ken was always around when I needed help and advice.

I would also like to thank Professor Don Fredericksen for his time and willingness to be on my committee, and my minor advisor Marilyn Rivchin who taught me how to shoot and edit motion pictures. Thanks also go to my advisor in applied physics, Professor Richard Lovelace, who helped bridge my career from physics to computer graphics.

Special thanks to Hurf Sheldon for helping set up the Measurement Laboratory, especially in completing the gonireflectometer. And sincere thanks to Sumant Pattanaik, Pete Shirley, Eric Lafortune, who taught me computer graphics rendering. I am grateful to all the friends in the Lab for various help and the many stimulating discussions. Also, thanks to my officemate Gordon Kindlmann for the company through the numerous hard working nights. Thanks to Jonathan

Corson-Rikert, Ellen French, Linda Stephenson for all the administrative support and sorting the bills for equipment purchases.

A major part of the gonioreflectometer presented in this thesis was donated by the Imaging Science Division of Eastman Kodak. Hewlett Packard Company donated the PC and workstations. The research conducted was supported by the NSF/ARPA Science and Technology Center for Computer Graphics and Scientific Visualization (ASC-8920219). The equipment in the Light Measurement Laboratory was funded by NSF Thermal System Program, under grant CTS-9213183.

Table of Contents

1	Introduction	1
1.1	Overview	1
1.2	Background	3
1.3	Thesis Organization	12
2	The Kodak Gonioreflectometer	13
2.1	The Original Kodak Design	13
2.2	Modification and Extension	16
2.3	Constraints of the Gonioreflectometer	19
3	Geometrical Considerations and Design	22
3.1	Motion Control	23
3.2	Coordinate Systems	23
3.3	Motor Rotation and Coordinate Transformation	25
3.4	Inverse Kinematics	27
3.5	Choosing Sample Positions on the Hemisphere	29
3.6	Optimization of Scan Path	31
4	Source and Viewing Optical Considerations and Design	35
4.1	Defining the Reflecting-Surface Area	35
4.2	Calibration and Normalization	38
4.3	Requirements for the Light Source	39
4.4	Detection of Reflected Radiance	41
4.4.1	Size of Test Sample	43
4.5	Polarization Biases of Source and Detector	44
5	The Light Source	47
5.1	Design And Components	48
5.2	Uniformity	50
5.3	Reciprocity	50

5.4	Stability	50
6	The Detector	53
6.1	Design	53
6.1.1	The Oriel Multispec/Instaspec II Spectroradiometer	54
6.1.2	Focusing Optics	55
6.2	Spectral Calibration	57
6.2.1	Spectral Resolution and Signal Noise	58
6.3	Polarization Bias	59
6.4	Radiometric calibration	60
6.5	Signal Processing	60
6.5.1	Detector Noise	60
6.5.2	Dynamic Range	62
7	Errors	64
7.1	Sources of Errors	65
7.2	Measured Signal	65
7.3	Noise Equivalent BRDF	67
7.4	Angular Accuracy	68
8	Calibration and Normalization	70
8.1	Relative Calibration Using A Diffuse Standard Reference	70
8.2	Absolute Calibration by Measuring The Direct Irradiance	74
9	Measurements and Results	76
9.1	Instrument Signature	78
9.2	Specular Reflectance	79
9.3	Bidirectional Reflectance	84
9.3.1	Spectralon	85
9.3.2	Blue Paint	90
9.3.3	Q Panel R-46, Stainless Steel	95
9.4	Directional Hemispherical Reflectance	96
10	Conclusion	103
10.1	Conclusion	103
10.2	Future Work	104
A	Specifications	106

B	Optical Alignment and Sensitivity	109
B.1	Aligning the Goniometric Stages	109
B.2	Aligning the Light Source and Detector	112
C	Operating Procedures and Precautions	114
D	Converting Raw Signals to BRDFs	118
E	Reciprocity Test	120
F	Sample Numerical Data	124
	Bibliography	128

List of Figures

1.1	Reflection geometry.	4
1.2	BRDF measurements of white (left) and black (right) samples by eighteen facilities.	10
2.1	Side view of the original Kodak Gonioreflectometer.	14
2.2	Bird's eye view of the original Kodak Gonioreflectometer.	15
2.3	Bird's eye view of the modified gonioreflectometer.	18
2.4	Block diagram showing the schematic of the measurement system.	19
2.5	Photograph of the gonioreflectometer.	20
3.1	Coordinates setup of the gonioreflectometer.	24
3.2	Rotated primed coordinates.	25
3.3	θ_3 is uniquely defined by the incidence and reflection direction.	28
3.4	Two sampling patterns for scanning the hemisphere.	30
3.5	Optimized scan path to scan the predetermined measurement posi- tions.	33
3.6	A magnified version of Figure 3.5.	34
4.1	Three ways of defining the reflecting surface, ΔA_r	36
4.2	Spectral polarization bias of an HLX lamp.	41
4.3	Optical configurations of illumination and radiance detection.	43
5.1	Schematic of the light source assembly.	48
5.2	Polarization bias of the light from the source assembly.	49
5.3	(a) Measurements of source intensity at various positions (shown in (b)) across the source beam. (b) Locations on the cross-section of the beam where measurements in (a) were made.	51
6.1	Schematic of the detector's focusing optics.	56
6.2	Plot of recorded points and fitted straight line for the array-diode wavelength calibration.	58
6.3	Polarization bias of the detector.	59

6.4	The Gaussian smoothing filter.	62
7.1	Estimated percentage error of BRDF measurement as a function of θ_i	66
7.2	Noise equivalent BRDF, assuming $\theta_i = 0^\circ$	68
9.1	Instrument signature at $\lambda = 650\text{nm}$	79
9.2	Measured BRDF of a vacuum coated aluminum mirror on the incidence plane, at incidence angle of 45° and at wavelength of 550nm	80
9.3	Comparison of polarized specular reflectance of a vacuum-coated aluminum mirror at an incidence angle of 45° , measured with the Optronic OL740-75M specular reflectometer and our gonioreflectometer.	82
9.4	Comparison of polarized specular reflection of a blue plastic at an incidence angle of 45° , measured with the Optronic OL740-75M specular reflectometer and our gonioreflectometer.	83
9.5	Measured BRDF (unpolarized) of Spectralon with source incident at $\theta_r = 0^\circ$, $\varphi_r = 0^\circ$, and view direction at $\theta_r = 45^\circ$, $\varphi_r = 180^\circ$	87
9.6	BRDF of Spectralon on the incidence plane at $\theta_i = 30^\circ$ for incidence source of p polarization, 633nm wavelength.	88
9.7	BRDF of Spectralon on the incidence plane at $\theta_i = 60^\circ$ for an incidence source of p polarization, 633nm wavelength.	89
9.8	BRDF of latex blue paint at a 450nm wavelength at incidence angles of 20° , 35° , 55° , and 65°	90
9.9	BRDF of latex blue paint at a 450nm wavelength, at incidence angles of 75° and 85°	91
9.10	Measured BRDF of the latex blue paint at $\theta_i = 55^\circ, 65^\circ, 75^\circ$, on the incidence plane.	93
9.11	Measured BRDF of the blue paint on the incidence plane at $\theta_i = 75^\circ$, and $\lambda = 450, 550, 650\text{nm}$	94
9.12	The same curves in Figure 9.11 plotted on a larger scale.	95
9.13	BRDF of the Q-Panel R-46, a matte-finished stainless steel, measured in two crossed incidence planes, at $\theta_i = 60^\circ$ and wavelength = 650nm	96
9.14	BRDF of Q-Panel R-46, measured in two crossed incidence planes at an incidence angle of 60°	97
9.15	Directional-hemispherical reflectance of the latex blue paint, plotted for various wavelengths as a function of incidence angle.	99
9.16	Directional-hemispherical reflectance of the latex blue paint as a function of wavelength at incidence angles of 20° , 55° , 75° , and 85°	100

9.17	Comparison of the directional-hemispherical reflectance of blue paint as measured by our gonireflectometer and by the Optronic OL 740-70.	101
E.1	Reciprocal measurements made of Spectralon sample.	123

List of Symbols

f_r	BRDF, bidirectional reflectance distribution function, [sr ⁻¹]
L_i	Incidence radiance, [W m ⁻² sr ⁻¹]
L_r	Reflected radiance, [W m ⁻² sr ⁻¹]
$L_{\lambda,i}$	Incidence spectral radiance, [W m ⁻³ sr ⁻¹]
$L_{\lambda,r}$	Reflected Intensity, [W m ⁻³ sr ⁻¹]
E_i	Irradiance, [W m ⁻²]
E_r	Reflected flux density, [W m ⁻²]
q_i	incidence energy flux, [W]
q_r	Reflected energy flux, [W]
V_r	Measured noise-free signal of reflected radiance. [signal counts/s]
Ω_i	Incidence solid angle, [sr]
Ω_r	Reflected solid angle, [r]
Ω_s	Irradiating source solid angle, [sr]
Ω_d	Detector solid angle, [sr]
ΔA_r	Reflecting surface on sample, [m ²]
ΔA_{r0}	Reflecting surface in normal direction, [m ²]
λ	Wavelength, [m]
\hat{s}_i	Incidence direction
\hat{s}_r	Reflection direction
\hat{n}	Normal vector on test sample
θ_i	Incidence angle from normal, [rad]
θ_r	Reflected angle from normal, [rad]
θ_r	Reflected angle from normal, [rad]
φ_i	Incidence azimuthal angle, [rad]
φ_r	Reflected azimuthal angle, [rad]
Ω_i	Incidence solid angle, [rad]
Ω_r	Reflected solid angle, [rad]
Ω_s	Irradiating source solid angle, [rad]
Ω_d	Detector solid angle, [rad]

Chapter 1

Introduction

1.1 Overview

The bidirectional reflectance distribution function (BRDF) is the physical property of material which describes the pattern of light reflected from a surface of the material into all directions above the surface, for an incident light beam coming from a particular direction. It is a five-dimensional function that governs the amount of light of a certain wavelength, coming from any direction, that is reflected in all possible directions. For a homogeneous surface, the BRDF determines the appearance of material in different view directions. Since the actual BRDF is a complicated multidimensional function, the simplifying models known as diffuse (Lambertian) reflectance and specular (mirror-like) reflectance are often used to describe the complete *reflectance*¹.

¹Note that the BRDF, unlike the *reflectance*, does not range from 0 to 1. The BRDF is a *reflected radiance* distribution function that ranges from 0 to ∞ .

Despite its complexity, the BRDF is used in physically based computer graphics global illumination computation to achieve simulation of high accuracy and fidelity [12] [26]. It is extensively used in the rendering works at the Cornell Program of Computer Graphics. Various models have been derived to simulate the BRDF of material on both a macroscopic and microscopic scale [32]. The He reflectance model [13] is a sophisticated analytical model based on physical optics and applies to isotropic materials. However, the model is cumbersome to compute and the values for the parameters required by the model are not always easily obtainable. To achieve scientific validity, a complex analytical reflectance model should be verified by measurements and experiments. Measurement is the most straightforward means for obtaining BRDFs and may be used for broad classes of materials, whereas models may be limited to narrow classes of materials. A device which measures BRDF is called a *gonioreflectometer* (*gonio* refers to the multiple direction capability of the instrument) and is the subject of this thesis.

The Light Measurement Laboratory in the Cornell Program of Computer Graphics was set up to improve physical realism of computer graphics rendering by providing the required light reflection and emission data [14][11]. The present author was responsible for equipment selection, purchase, set up and testing for the Light Measurement Laboratory as part of an earlier study [11]. A gonioreflectometer was listed as a high priority piece of equipment for establishing the facility. In December 1993, a partially completed gonioreflectometer, designed and built by Mr. Larry Iwan² at the Imaging Science Division of Eastman Kodak, was donated to the Light

²According to Mr. Iwan, the equipment was constructed for verifying the usefulness

Measurement Laboratory.

This thesis describes the extension and modification of the Kodak instrument to become an automated three-axis gonioreflectometer capable of measuring the BRDF of isotropic surfaces over the entire hemisphere of incidence and reflection directions above a surface and in the entire visible wavelength range. The final design of the gonioreflectometer, and some of its resulting measurements of BRDF, are presented.

1.2 Background

The geometry of the bidirectional reflection process is depicted in Figure 1.1. A surface is shown illuminated from a direction (θ_i, φ_i) by a cone of radiation centered within a solid angle $d\Omega_i$, with reflection in the direction (θ_r, φ_r) , centered within a cone $d\Omega_r$. The bidirectional reflectance distribution function (BRDF) is defined as the ratio of the directionally reflected *radiance* to the directionally incident *irradiance*. *Radiance* is the radiant energy flow per unit solid angle and unit area normal to the rays and has the units $[\text{Wm}^{-2}\text{sr}^{-1}]$. *Spectral radiance* is the radiance per unit wavelength interval and has units $[\text{Wm}^{-3}\text{sr}^{-1}]$. The *irradiance* is the power flux density irradiating a surface per unit (unprojected) area of the surface and has units $[\text{Wm}^{-2}]$. For the cone-surface geometry of Figure 1.1, the area normal to the ray is calculated as $\cos\theta_r dA$ for the cone of reflection and $\cos\theta_i dA$ for the cone of incidence. The *spectral irradiance* is the incident irradiance expressed in per-unit

of the He reflection model for Kodak. Mr. Iwan is now with the University of Rochester Laser Laboratory.

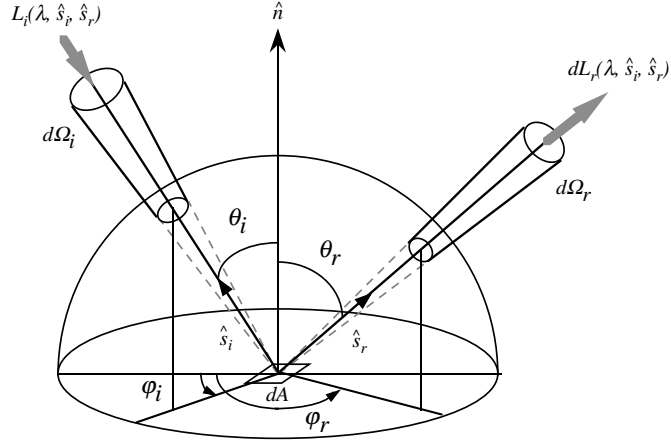


Figure 1.1: Reflection geometry showing cones of incident and reflected light above a surface element.

wavelength interval with units $[\text{Wm}^{-3}]$.

In terms of the foregoing quantities, the BRDF is defined as a function of wavelength by [22]:

$$f_r(\lambda, \hat{s}_i, \hat{s}_r) = \frac{dL_{\lambda,r}(\lambda, \hat{s}_i, \hat{s}_r)}{dE_{\lambda,i}(\lambda, \hat{s}_i)}$$

where $dE_{\lambda,i}$ is the incident spectral irradiance, and $dL_{\lambda,r}$ is the reflected spectral radiance. Note that the BRDF is reciprocal [22] [24]. If the incident and reflected directions are reversed, the function has the same value. Further, the radiance does not vary along the direction of propagation of a ray, in the absence of out-scattering or in-scattering along the ray. This will allow us to measure the reflected radiance at any distance from the reflecting surface.

For simplicity, we will omit the wavelength and polarization notation in the

equations that follow. In a measurement system, each wavelength measurement is essentially integrated over a finite bandwidth of radiation, $\Delta\lambda$. After the wavelength notation is dropped, the BRDF becomes:

$$f_r(\hat{s}_i, \hat{s}_r) = \frac{dL_r(\hat{s}_i, \hat{s}_r)}{dE_i(\hat{s}_i)}$$

where, at any particular wavelength λ_0 , it will be understood that the radiance $L_r \approx L_{\lambda,r}(\lambda_0, \hat{s}_i, \hat{s}_r)\Delta\lambda$ and the irradiance $E_i \approx E_{\lambda,i}(\lambda_0, \hat{s}_i)\Delta\lambda$.

With $d\Omega_i$ as the incident solid angle, the *irradiance* dE_i may be expressed in terms of an *incident radiance* L_i as

$$dE_i(\hat{s}_i) = \cos\theta_i L_i(\hat{s}_i) d\Omega_i$$

The cosine term serves to project the surface area in the incident direction \hat{s}_i . Note that the incident radiance L_i is not a differential, but a finite quantity. Similarly, the outgoing *reflected power density* leaving the surface, per unit area of the surface, in the cone $d\Omega_r$, can be expressed in terms of the outgoing *reflected radiance* by

$$d^2E_r(\hat{s}_i, \hat{s}_r) = \cos\theta_r dL_r(\hat{s}_i, \hat{s}_r) d\Omega_r$$

Note that the reflected energy is a second order differential. This denotes the obvious fact that an incident energy flux dE_i is directionally scattered to all directions in the hemisphere above the scattering surface, leading to a smaller directionally reflected energy, d^2E_r .

With the BRDF known, and with a surface illuminated over the entire hemisphere of incidence angles, the reflected radiance *in a particular direction* above

the surface may be found by integrating the definition of BRDF over the incident hemisphere:

$$L_r(\hat{s}_r) = \int_{\Omega_i} f_r(\hat{s}_i, \hat{s}_r) L_i(\hat{s}_i) \cos \theta_i d\Omega_i$$

If the incident radiance $L_i(\hat{s}_i)$ is uniform over all incidence directions, we thus obtain the *hemispherical-directional reflectance* as

$$\rho_{hd}(\hat{s}_r) = \frac{L_r(\hat{s}_r)}{L_i} = \int_{\Omega_i} f_r(\hat{s}_i, \hat{s}_r) \cos \theta_i d\Omega_i$$

which can be used for uniform hemispherical illumination and directional reflection.

On the other hand, for incidence in a particular cone of directions, the energy dE_r , reflected to the *entire* hemisphere of reflection angles may be found by integrating the reflected differential energy, d^2E_r , over the solid angles of reflection. Using the definition of BRDF, we can write the reflected power density as

$$dE_r(\hat{s}_i) = \int_{\Omega_r} f_r(\hat{s}_i, \hat{s}_r) dE_i(\hat{s}_i) \cos \theta_r d\Omega_r$$

Taking dE_i as constant over the incident cone, we obtain the *directional-hemispherical reflectance* as

$$\rho_{dh}(\hat{s}_i) = \frac{dE_r(\hat{s}_i)}{dE_i(\hat{s}_i)} = \int_{\Omega_r} f_r(\hat{s}_i, \hat{s}_r) \cos \theta_r d\Omega_r$$

The hemispherical reflectances satisfy the reciprocity condition

$$\rho_{hd}(\hat{s}) = \rho_{dh}(\hat{s})$$

Later in this thesis we will use spectrally measured hemispherical reflectances to check our measured BRDFs.

In a measurement system, the reflecting area and receiver solid angle are not infinitesimal but finite, so $dA \rightarrow \Delta A$ and $d\Omega_r \rightarrow \Delta\Omega_r$. The reflecting energy flux, d^2q_r , sensed by an imaging detector with an aperture defining the receiving solid angle $\Delta\Omega_r$ and sampling area ΔA , is thus given by

$$\begin{aligned} d^2q_r(\hat{s}_i, \hat{s}_r) &= \int_{\Delta A} d^2E_r dA \\ &= \int_{\Delta\Omega_r} \int_{\Delta A} dL_r(\hat{s}_i, \hat{s}_r) \cos\theta_r dA d\Omega_r \end{aligned}$$

which is an integral of dL_r over $\Delta\Omega_r$ and ΔA . If dL_r is taken as a constant over $\Delta\Omega_r$ and ΔA , and $\cos\theta_r$ is evaluated as a midpoint value, the BRDF can be estimated from

$$f_r(\hat{s}_i, \hat{s}_r) = \frac{1}{\cos\theta_r \Delta A \Delta\Omega_r} \frac{d^2q_r(\hat{s}_i, \hat{s}_r)}{dE_i(\hat{s}_i)}$$

Two measurement procedures are used in the present thesis: In the *absolute* method, the previous equation is used, with d^2q_r and dE_i measured separately as signals and then ratioed. (This requires a detector with a large dynamic range.) The parameters $\cos\theta_r$, ΔA , and $\Delta\Omega_r$ are obtained from the measurement geometry. In the *comparative* method, a sample with a known directional hemispherical reflectance is used. Measurement scans are carried out over the entire hemisphere above the sample for the specific incidence angle where the hemispherical reflectance is known. The measurements are integrated (scaled appropriately according to the reflection directions) and the calibration factor to convert the measurement to BRDF is calculated from the ratio of the integral to the known reflectance. The details are given in Chapter 8.1.

The size of the reflecting area is important and must be selected according to the surface area of concern. For example, in computer graphics, rendering with the measured BRDF of a rough or grainy surface whose graininess is visible to the eye (e.g. coarse fabric), will not produce a grainy effect, since the measurement might be over an area encompassing many of the rough elements or grains. The solid angle of the detector should also be small enough to capture sufficient angular resolution, and to enable measurements of reflection at high grazing angles where interesting off-specular and highly directional scattering phenomena can occur [30].

In our pursuit to measure BRDF for computer graphics rendering, we ignore the rare cases of non-linear, intensity dependent effects of reflection that can be encountered in certain materials. Reflection is only one kind of interaction of light with surfaces. Strictly speaking, reflection refers to the process by which a radiant flux incident on a surface leaves the surface on the same side as the incident without a change in frequency. As pointed out in [24], the flux produced by *fluorescence* is not *reflected flux*. Fluorescence, which is present in a lot of materials, is the process by which an incident radiant energy is absorbed by the material and is re-emitted at a different wavelength. The re-emission may not be instantaneous, and if it persists, it is called *phosphorescence*. The measurement of BRDF, however, is strictly a measurement of reflection. Measuring the light-surface-interaction properties of fluorescent material is more complicated and differs from a conventional BRDF measurement.

A definition of BRDF has been given by Nicodemus *et al.* in [24], which has become a standard for reflectance nomenclature. Nicodemus also provided a very

general discussion of various optical configurations for BRDF measurements. Many gonioreflectometers have been documented [25] [19]. An example of a gonioreflectometer is one at the former National Bureau of Standards, described in [15]. It is a laser-source bidirectional reflectometer which takes into account polarization, adjusting with integrating spheres, and [15] provides details in the alignment and implementation of their instrument.

BRDF can be difficult to measure. Eighteen facilities participated in a BRDF round robin organized by Tom Leonard in 1988 [18] where four two-inch diameter samples of a white diffuse surface, a black diffuse surface, an industrial grade molybdenum mirror, and an aluminum mirror were measured. The results showed an enormous range of variation. Measurements of the black and white samples made by the different facilities are shown in Figure 1.2. The figures are adopted from page 234 of [18]. Leonard subsequently compiled a list of the causes of BRDF measurement errors, and made suggestions for improved measurement accuracy [17], which aided the establishment of ASTM Standards E1392-90 “Standard Practice for Angle Resolved Optical Scatter Measurements On Specular or Diffuse Surfaces.” Leonard’s paper [17] provides a checklist for designing a gonioreflectometer. The Commission Internationale de l’Eclairage (CIE) has also specified some preferred BRDF reference standard configurations. [28] contains much additional information on optical scattering and measurement.

A classic example of a gonioreflectometer is one designed and constructed by Torrance in 1965 that supported the development of the Torrance-Sparrow reflectance model [29], which was later adopted by Blinn in computer graphics [2]. The later

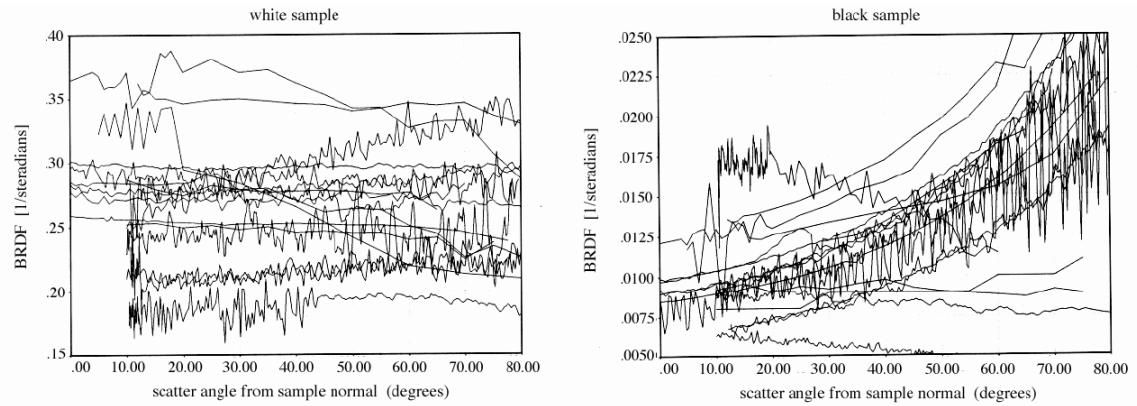


Figure 1.2: BRDF measurements of white (left) and black (right) samples, at 633nm wavelength, by eighteen facilities. The specular direction is at 10° . The white sample has a flat BRDF and the black sample shows increasing reflectance at large angles. [From page 234, [18].]

Cook model [5] and He model have ties back to the results from Torrance's gonireflectometer. Although unautomated, it was a mechanically elegant and precise instrument. Further, it was a three-axis instrument capable of measuring the BRDF of anisotropic surfaces; the Eulerian rotation of the source together with the change in coordinates of the reflection direction allowed the source azimuth direction to be held constant. This is a geometric capability the gonireflectometer discussed in this thesis has failed to achieve. Similar to the three-axis gonireflectometer at RIT [10], which provided measurements for the Cornell Program of Computer Graphics before the establishment of the Light Measurement Lab, our instrument assumes a test sample to be isotropic, and allows the absolute azimuth incidence direction to vary while all reflection measurements are made relative to the incident

direction. However, with the possible addition of a fourth degree of rotation, our gonioreflectometer could be extended to make measurements of anisotropic BRDF.

In the field of computer graphics, Ward constructed an imaging gonioreflectometer that allows BRDF of anisotropic surfaces to be measured in a few minutes [31]. The imaging gonioreflectometer utilizes a camera with a fish eye lens, that views the interior of a hemispherical mirror receptor. This lens captures the entire reflected radiation of a directionally illuminated sample. The configuration of the system is similar to the apparatus Coblentz used to measure directional-hemispherical reflectance as described in [7], except that the detector is replaced by a wide angle CCD camera. The idea and the design of Ward's apparatus is very clever, but the optics are poorly defined. Near specular or specular reflectance cannot be measured, and near grazing angle measurement cannot be achieved. Despite all its technical problems, the imaging gonioreflectometer is fast and provides some usable measurements for computer graphics. To generate BRDF data for use in computer graphics, a gonioreflectometer should be fast to be of practical use.

Dana *et al.* constructed a goniophotometer that uses a robot arm to hold and rotate the test sample, and a video camera to detect [6] the reflections. Measurements of three RGB channels (which are claimed to be 8 bits each) are made. The equipment was calibrated with reference to a Photoresearch SpectraScan PR-704. The problem with using a video camera as a detector is that video cameras are noisy and the radiometric linearity of the CCD may not be preserved when transferred as video signal. Also, the RGB filters may possibly be different from the three-channel RGB filters in the Photoresearch PR-704, which can result in inconsistent calibra-

tion. The goniophotometer that Dana *et al.* constructed calculates the BRDF from a 2-D radiance image of the test sample. This allows multi-scale BRDF calculations to be carried out. Dana *et al.* also measure a bidirectional texture function (BTF) simultaneously. The resulting database of measurements is available online from Columbia University.

1.3 Thesis Organization

This thesis describes the design, principles, and fabrication of a working gonioreflectometer capable of measuring the BRDF of isotropic materials. The next chapter, Chapter 2, provides a background on the original design of the instrument from Kodak, and the modifications necessary to extend and complete the instrument. Chapter 3 provides a discussion of the mechanical design and kinematics of the instrument. Chapter 4 presents a discussion of the geometrical optics involved in the measurement. Chapter 5 and 6 contain the details of the light source and detector, respectively. Chapter 7 contains a discussion of the deterministic error and estimated systematic errors in BRDF measurement. Chapter 8 presents the detailed mathematical derivation of the calibration procedures used in our calculation of BRDF from raw measurements. Chapter 9 describes some measurement results of various materials and their comparisons to measurements made at other facilities. Chapter 10 is the conclusion. The specifications of our gonioreflectometer, operating instructions, design diagrams, and sample numerical data are provided in the appendices.

Chapter 2

The Kodak Gonioreflectometer

In December 1993, a goniometric stage was donated to the Light Measurement Laboratory by the Imaging Science Division of Eastman Kodak. The instrument¹ was part of a gonioreflectometer designed by Mr. Larry Iwan. It was supplied without a light source, wavelength scanning detector, or control computer.

This chapter describes the Kodak gonioreflectometer. Here, we also discuss the additional work needed to extend and modify the gonioreflectometer to become a functional measurement apparatus.

2.1 The Original Kodak Design

The Kodak *gonioreflectometer*, as received, consisted of a two-axis gonio-stage (two stages, one mounted on another) for holding and rotating a test sample. The two

¹Mr. John Schoff was the support specialist at Kodak who helped to fabricate the instrument.

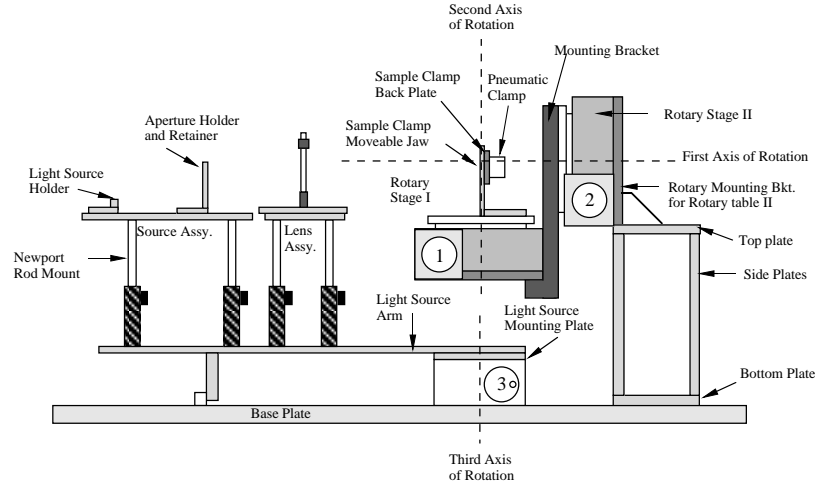


Figure 2.1: Side view of the original Kodak Gonioreflectometer.

stages were controlled by two stepper motors driven separately by a motor controller. There was a third manual stage for rotating an arm that supported a light source. Figure 2.1 and Figure 2.2 show the schematics of the instrument layout. The stages and the source arm were mounted on a black anodized aluminum base plate (28in. \times 36in. \times 1in.). The motor controller, called the MAC200, manufactured by Techno/Designatronics, Inc., in New Jersey, accepts ASCII commands via RS-232.

We refer to the two goniometric stages as Stage I and Stage II. Stage II was mounted on a support platform that was suspended above the center of the aluminum baseplate. The axis of rotation was horizontal. Stage I was mounted on Stage II over two long suspending bars, with its axis always perpendicular to the axis of Stage II. Stage I revolves around the axis of Stage II. A sample was to be

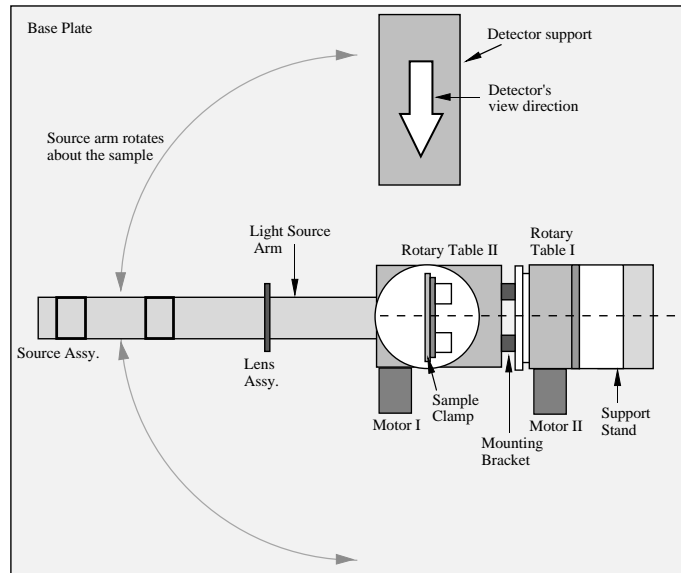


Figure 2.2: Bird's eye view of the original Kodak Goniometer.

mounted on Stage I, with the axis of rotation lying in the plane of the sample surface. The light source arm moved parallel to the base plate, on a roller, and rotated about a vertical axis that intersected the common intersection of the first two axes. A wavelength scanning detector had been mounted in a fixed position on the base platform, viewing the sample at a distance to one side of the stages.

2.2 Modification and Extension

The following steps were taken to modify and complete the gonireflectometer.

1. The entire goniometric stage was re-mounted on a 5ft. \times 5ft. black polyurethane-coated optical breadboard² (Newport XSD-45). The large platform is needed to support the gonio-stage, and to accommodate both the detector and the rotating arm for the light source. It also damps vibrations.
2. The light source arm was replaced by a 36-inch optical rail (Newport URL-36). Mounting plates were fabricated to attach the rail to the existing rotation stage. An additional Techno stepper motor was added to automate and drive the source arm.
3. An unpolarized focusing light source was designed and constructed. The light source is mounted on the far end of the source arm. Details of the light source design will be discussed in Chapter 5.

²A breadboard is an optically flat working platform with mounting screw holes and internal damping structures.

4. The pneumatic sample holder on the original Kodak gonioreflectometer was removed, since it restricted the illuminated area on the sample. It also blocked the illuminating light at large incidence angles (grazing angles).
5. A new sample mount of larger size was constructed. The new mount allows illumination on the sample at large grazing angles ($\approx 86^\circ$) without occlusion. A fourth rotation stage can also be attached in the future to enable BRDF measurements of anisotropic materials.
6. Stage I was re-mounted with the stepper motor closer to Stage II. This move prevents the motor from blocking the sample from the source or the detector at certain orientations. The remounting also extends the “cradle-stage” (Stage I) farther from the the center of rotation of Stage II, thereby extending the non-self-occluding region.
7. An array diode spectroradiometer and focusing optics were integrated into the gonioreflectometer as a detector. A folding mirror is used to intercept the reflected light beam from the sample and to direct the beam to the spectroradiometer. Details of the detector are discussed in Chapter 6.
8. Programs were written to enable a PC compatible HP Vectra 486/66ST to control the array diode detector and the three stepper motors and to automate the measurement of the BRDF for isotropic samples.

Remounting the gonioreflectometer on the 5ft. \times 5ft. breadboard and extending the length of the source arm provided longer illumination and view distances. The

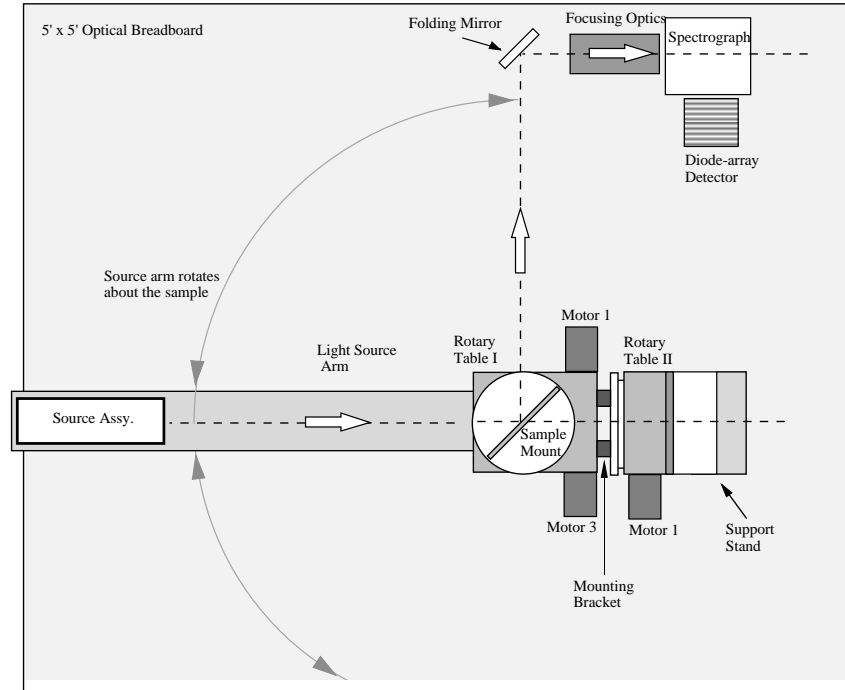


Figure 2.3: Bird's eye view of the modified Gonioreflectometer. The white arrows indicate the direction of illumination and reflection.

solid angles for illumination and reflection were decreased from the original Kodak design. This allows the illumination and reflection angles to approach grazing angles with respect to the surface of a sample. With a sample that is sufficiently large, vignetting problems [17] can be avoided. Figure 2.3 shows the modified gonioreflectometer from a bird's eye view. A schematic of the measurement system is depicted in Figure 2.4. A photograph of the complete gonioreflectometer is shown in Figure 2.5.

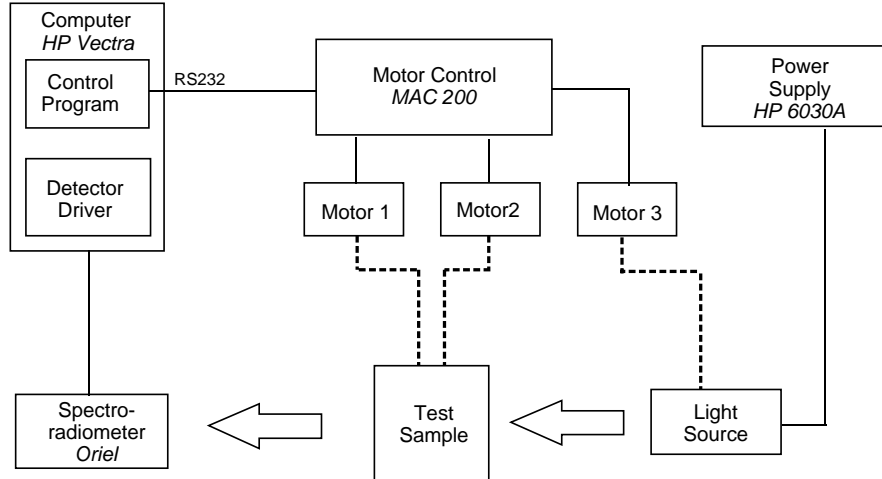


Figure 2.4: Block diagram showing the schematic of the measurement system.

2.3 Constraints of the Gonioreflectometer

The gonioreflectometer, as it was designed and later modified, can only measure the reflectance of isotropic samples since there are only three rotational degrees of freedom. The way the stages are mounted, neither the illuminating angle nor a reflection angle can be held fixed while carrying out a bi-hemispherical scan. Reflection angles are always measured with respect to the direction of illumination. However, it is possible that the system be further modified to allow anisotropic measurements by the addition of a fourth rotational degree of freedom.

Special procedures are required to align the optical pathways of the reflectometer, and to set the zeros of the computer controlled stepper motors. The largest misalignment error arises from the ruggedness of the mechanical hardware. The

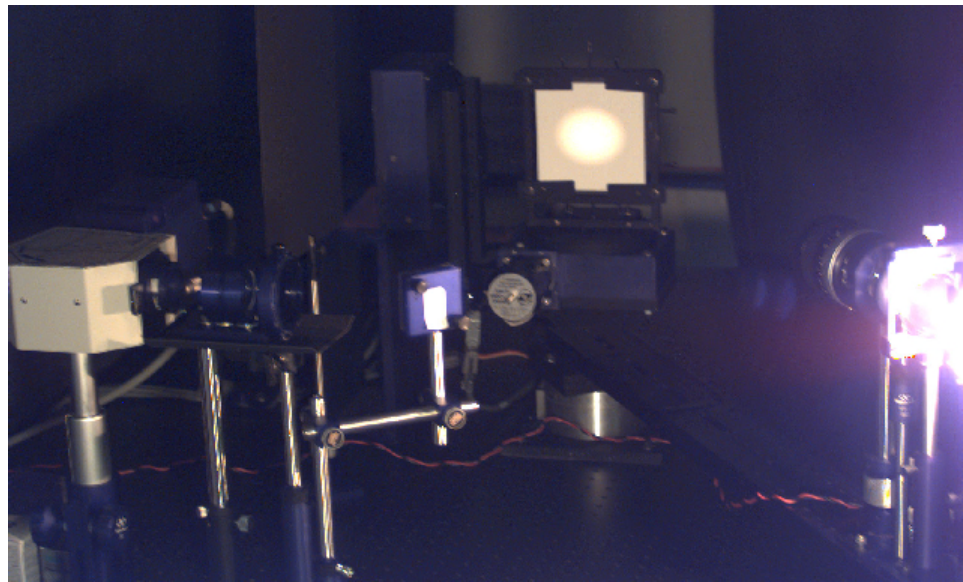


Figure 2.5: The gonioreflectometer with its detector optics (left) and light source optics (right) exposed. A white Spectralon sample (middle) is shown illuminated by the source at $\theta_i = 45^\circ$. The detector is viewing the sample via the folding mirror at $\theta_r = 0^\circ$.

load of Stage I with the sample mount mounted to Stage II causes the rotating shaft of Stage II to “bend” slightly. Actually, the shaft itself is very strong, but the components of the stage cannot be tightly assembled. As the Stages are rotated to various positions, the bending varies, thereby upsetting the center rotation of the sample. A major hardware modification would be required to rectify this fault. Otherwise, such mechanical error can be systematically characterized.

Chapter 3

Geometrical Considerations and Design

The gonioreflectometer presented in this thesis is a three-axis system. The three axes and optical equipment are sketched in Figure 3.1. A photograph is shown in Figure 2.5; the test sample, light source, and detector are in similar locations in Figure 2.5 and Figure 3.1. The sample mount has two degrees of freedom in rotation and the light source arm independently revolves around the sample mount. The light source emits a close-to-parallel beam focused at infinity, aimed at the center of the test sample, resulting in a close-to-zero illumination solid angle. The detector is stationary, and views the test sample via a folding mirror which bends the view path by 90° . The detector's external optics focus the center of the test sample on the detector's entrance slit. The receiving solid angle of the detector thus defined by the aperture of the detector's focusing optics. The details of the light

source and detector will be discussed in later chapters.

The goniometric geometry, its restrictions, and the motion control of the the gonioreflectometer are described in this chapter. The forward and inverse kinematics used to transform between the lab coordinates and the coordinates in the test sample's reference frame are discussed. We also discuss how the sampling locations (measurement locations) on the hemisphere above the sample's surface are chosen and the scan path used to optimize the measurements.

3.1 Motion Control

The rotation of the sample and the light source arm is controlled by three stepper motors, each with a torque of 110 N/m. The stepper motor controller and power supply, called the MAC2000, is manufactured by Techno Designatronics, and accepts ASCII commands via RS232 from a PC. The appropriate rotation speed and acceleration were chosen for each motor on each stage, to avoid vibrations and resonance. All the motors turn at 200 steps per revolution. The detailed mechanical specifications are given in Appendix A.

3.2 Coordinate Systems

Figure 3.1 shows the rotational axes of the gonioreflectometer corresponding to the three stepper motors. Two coordinate systems are shown. The primed coordinates are in the test sample's reference frame, with the z' -axis as the normal on the

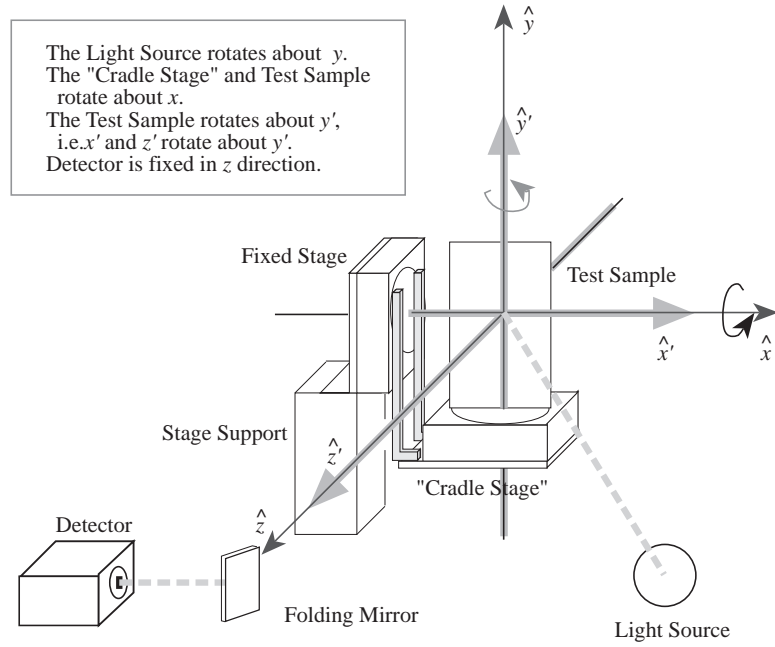


Figure 3.1: Coordinates setup ($\theta_1 = \theta_2 = \theta_3 = 0$) of the gonioreflectometer. All stages and motors are at home positions.

sample's surface. The unprimed coordinates are in the stationary laboratory frame. When all the motors are in their home positions ($\theta_1 = \theta_2 = \theta_3 = 0^\circ$), the two coordinate systems coincide and the sample surface normal (\hat{z}') points towards the detector through the folding mirror. In Figure 3.1, the two coordinate systems coincide; the motors are all in their home positions. Rotated coordinates are shown in Figure 3.2. The light source rotation is relatively straightforward and is not illustrated in the diagrams.

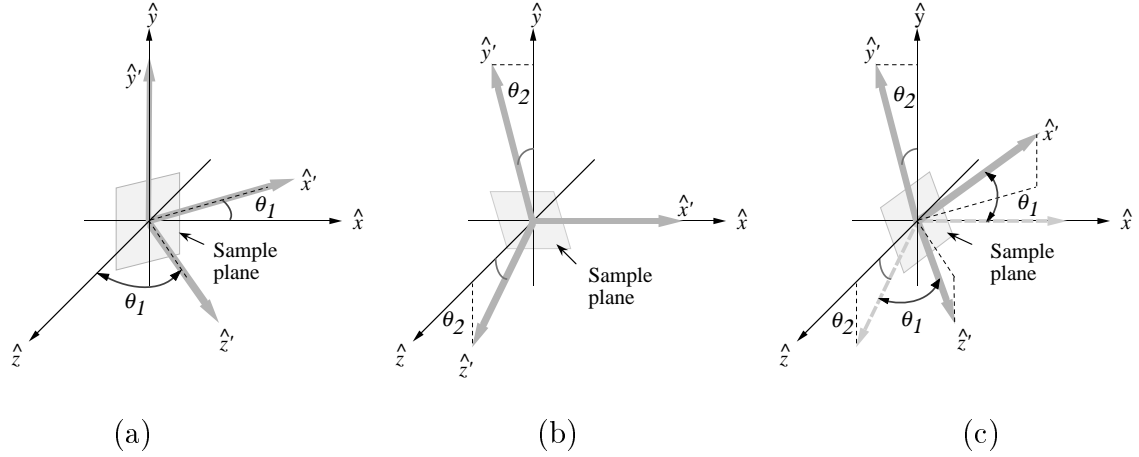


Figure 3.2: Rotated primed coordinates. Figure (a) shows only θ_2 has been rotated; Figure (b) shows only θ_1 rotation; and (c) shows both θ_1 and θ_2 rotated. The sequence of rotation does not matter in our case.

3.3 Motor Rotation and Coordinate Transformation

The operational range for each motor rotation is set as follows:

1. We set the range for motor 3 (θ_3) to be from 8° to 180° . This allows the light source to rotate 180° about \hat{y} . 8° is the upper mechanical offset beyond which the light source assembly will collide with the detector's receiving optics.
2. Motor 2 (θ_2) is restricted such that it can only turn from 0° to 180° . This allows the “cradle-stage” to rotate 180° about \hat{x} . Within these two quadrants, there is a region ($\sim 47^\circ - \sim 133^\circ$) where the light source will be occluded by the stage from the sample when $\theta_3 > 158^\circ$. The third and fourth quadrants are not used because *both* the light source and the detector can be blocked in

a similar region ($\sim 225^\circ - \sim 315^\circ$).

3. Motor 1 (θ_1) is allowed to turn freely about \hat{y}' , from 0° to 360° . This rotation has the least mechanical load and can be set to a relatively fast speed.

The following are the relations between a vector defined in the laboratory frame coordinates, \vec{r} , and the same vector defined in the sample frame coordinates, \vec{r}' , and vice versa:

$$\begin{aligned}\vec{r} &= T\vec{r}' \\ \vec{r}' &= T^t\vec{r}\end{aligned}$$

where T is the matrix that transforms a vector in the sample frame to a vector in the laboratory frame. We can think of T as being composed of two rotational transformations: R_y , rotation about \hat{y}' ; and R_x , rotation about \hat{x} . T' transforms coordinates in the lab frame to coordinates in the sample frame.

$$T = R_x R_y = \begin{pmatrix} 1 & 0 & 0 \\ 0 & \cos \theta_2 & -\sin \theta_2 \\ 0 & \sin \theta_2 & \cos \theta_2 \end{pmatrix} \begin{pmatrix} \cos \theta_1 & 0 & \sin \theta_1 \\ 0 & 1 & 0 \\ -\sin \theta_1 & 0 & \cos \theta_1 \end{pmatrix}$$

$$T' = T^t = \begin{pmatrix} \cos \theta_1 & \sin \theta_1 \sin \theta_2 & -\sin \theta_1 \cos \theta_2 \\ 0 & \cos \theta_2 & \sin \theta_2 \\ \sin \theta_1 & -\cos \theta_1 \sin \theta_2 & \cos \theta_1 \cos \theta_2 \end{pmatrix}$$

where T^t is the transpose of T . Since the detector is fixed in the \hat{z} direction and the light source always rotates about \hat{y} , the detector or reflection direction, \vec{r}_r , and source/incidence direction, \vec{r}_i , can be written as:

$$\vec{r}_r = \begin{pmatrix} 0 \\ 0 \\ 1 \end{pmatrix}, \quad \vec{r}_i = \begin{pmatrix} \sin \theta_3 \\ 0 \\ \cos \theta_3 \end{pmatrix}$$

$$\begin{aligned} \vec{r}'_r &= T' \vec{r}_r = \begin{pmatrix} -\sin \theta_1 \cos \theta_2 \\ \sin \theta_2 \\ \cos \theta_1 \cos \theta_2 \end{pmatrix} \\ \vec{r}'_i &= T' \vec{r}_i = \begin{pmatrix} \cos \theta_1 \sin \theta_3 - \sin \theta_1 \cos \theta_2 \cos \theta_3 \\ \sin \theta_2 \cos \theta_3 \\ \sin \theta_1 \sin \theta_3 + \cos \theta_1 \cos \theta_2 \cos \theta_3 \end{pmatrix} \\ &= \begin{pmatrix} \sin \theta'_i \cos \varphi'_i \\ \sin \theta'_i \sin \varphi'_i \\ \cos \theta'_i \end{pmatrix} \end{aligned}$$

For a sample that has an assumed isotropic surface, we ignore the true value of φ'_i and measure all φ'_r from φ'_i .

3.4 Inverse Kinematics

Although the preceding equations correctly describe the transformation of \hat{r}_i and \hat{r}_r in the sample frame to \hat{r}'_i and \hat{r}'_r in the laboratory frame, respectively, they are difficult to solve for θ_1 , θ_2 , and θ_3 , given θ_i , φ_i , θ_r , and φ_r as known variables. The inverse kinematics are carried out as follows:

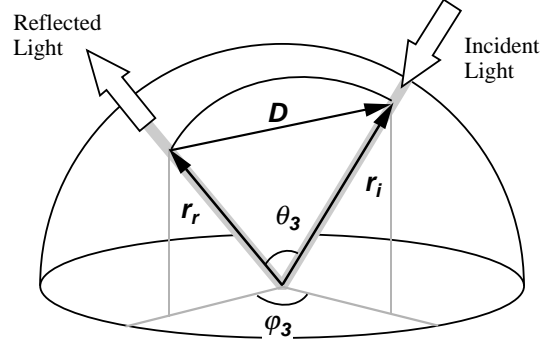


Figure 3.3: θ_3 is uniquely defined by the incidence and reflection direction.

We know that θ_3 is unique for any \hat{r}_i and \hat{r}_r , since θ_3 is the angular difference between the two vectors. Therefore, the magnitude of D in the equation below is unique.

$$|\hat{r}'_i - \hat{r}'_r| = |\vec{D}|$$

In the above equation, φ_i is always assumed to be zero. And since the hemisphere has a unit radius,

$$\begin{aligned}\cos(\theta_3) &= 1 - D^2/2 \\ \theta_3 &= \cos^{-1}(1 - D^2/2)\end{aligned}$$

From the previous section, we know that

$$\begin{aligned}\cos \theta_i &= \sin \theta_1 \sin \theta_3 + \cos \theta_1 \cos \theta_2 \sin \theta_3 \\ &= \sin \theta_1 \sin \theta_3 + \cos \theta'_r \sin \theta_3\end{aligned}$$

where $\cos \theta'_r = \cos \theta_1 \cos \theta_2$.

$$\implies \theta_1 = \sin^{-1} \left(\frac{\cos \theta'_i - \cos \theta'_r \cos \theta_3}{\sin \theta_3} \right)$$

There is no solution for θ_1 if $\cos \theta'_i - \cos \theta'_r \cos \theta_3 > \sin \theta_3$. Once θ_1 is found, θ_2 is calculated as follows:

$$\theta_2 = \cos^{-1} \left(\frac{\cos \theta'_r}{\cos \theta_1} \right)$$

The correct θ_1 and θ_2 from the multiple solutions are chosen by checking their associated φ'_r values.

It is conceivable that anisotropic measurement is possible if we have a fourth rotary stage, located where the test sample is mounted, such that the absolute φ'_i with respect to the sample surface can be kept constant by turning the test sample about the sample normal, \hat{n} . Then φ'_r , measured from the stationary φ'_i , is the absolute φ'_i with respect to the sample surface and φ'_i is always zero.

3.5 Choosing Sample Positions on the Hemisphere

Measurement can be made for any incidence angle (θ_i) from 0° to 86° . For every selected incidence angle, we choose the corresponding outgoing/reflection directions (θ_r, φ_r) where we will take measurements, on the hemisphere above the sample. We then compute the corresponding motor positions $(\theta_1, \theta_2, \text{ and } \theta_3)$.

There are two sampling patterns that we use. The first has all the sampling positions distributed evenly over the hemisphere and the second has samples densely clustered towards the specular direction. When measurements over the hemisphere

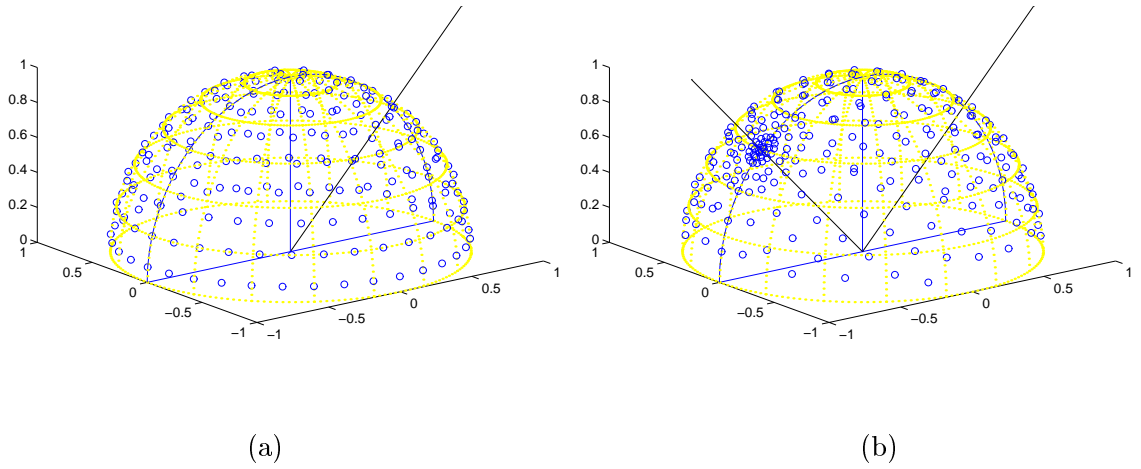


Figure 3.4: Two sampling patterns on the hemisphere are shown. (a) shows an evenly distributed positions with equal solid angles, and (b) shows a pattern with sample positions concentrated towards the specular direction. Incidence and reflection directions, indicated by solid lines, lie on the incidence plane. Incidence angle is at 45° .

are to be integrated to obtain the hemispherical reflectance, the first pattern is used. Figure 3.4 (a) and (b) show two sets of predetermined sparse-sampling locations on the hemisphere. (a) is a generic “evenly” spaced sample distribution, with approximately 5° separation between the samples. There are a total of 208 samples on the hemisphere. A denser sampling can also be used for higher spatial resolution. Figure 3.4(b) shows 240 sampling locations with increasing spatial density towards the specular (incidence and specular reflection direction are indicated by solid lines) direction. A high angular resolution is preferred around a region of high reflectance gradient. The user can choose any sampling pattern he or she desires. The sampling locations have to be precomputed and saved in a file to be read by the control software.

3.6 Optimization of Scan Path

After all the desired measurement positions on the hemisphere have been determined, we determine the optimal order for scanning these positions by using one of the two schemes described below. We optimize the scan path by attempting to join all the scattered positions by the shortest line possible, taking into account the mechanical loads and speeds of the motors. This is a “traveling salesman” problem for which there is no general solution. Scheme 1 is a general scheme we use when all the predetermined positions are randomly distributed.

Scheme 1:

1. All the predetermined positions are sorted first, by ascending θ_3 , since motor 3 is the slowest.
2. We select an optimal θ_3 interval, $\Delta\theta_3$, and segment all the sorted positions. Within every $\Delta\theta_3$, we again sort the positions by θ_2 .
3. The sorting orders of θ_2 are alternated, from one $\Delta\theta_3$ interval to the next.
4. θ_1 moves the fastest and therefore is not given any sorting priority.

Since we know the rotation speeds of the individual motors and the motor-to-stage rotation ratios (steps/°), we can integrate the motors’ rotation times, and compute the total travel-time required to scan through all the sorted positions. The optimal $\Delta\theta_3$ is one that would give the minimum total travel time.

Scheme 2 is advantageous when θ_2 's are clustered toward the upper and lower regions of θ_2 's range. Scheme 2 also has the advantage that motor 3 will return to a position near where the scan begins.

Scheme 2:

1. Sort all motor positions (θ 's) in ascending order of θ_2 's.
2. Divide all the sorted positions into two segments with the demarcation at $\theta_2 = 90^\circ$.
3. Sort all positions in the first segment in ascending θ_3 .
4. Sort all positions in the second segment in descending θ_3 .

Figure 3.5 and Figure 3.6 show the path taken to span the predetermined sample positions on the hemispherical space above a test sample's surface. The three axes represent the three motors' positions, scaled by their individual speed, and represent the required durations to reach the position starting from 0. The shorter the scan path to connect all the points together, the sooner the measurements will be completed.

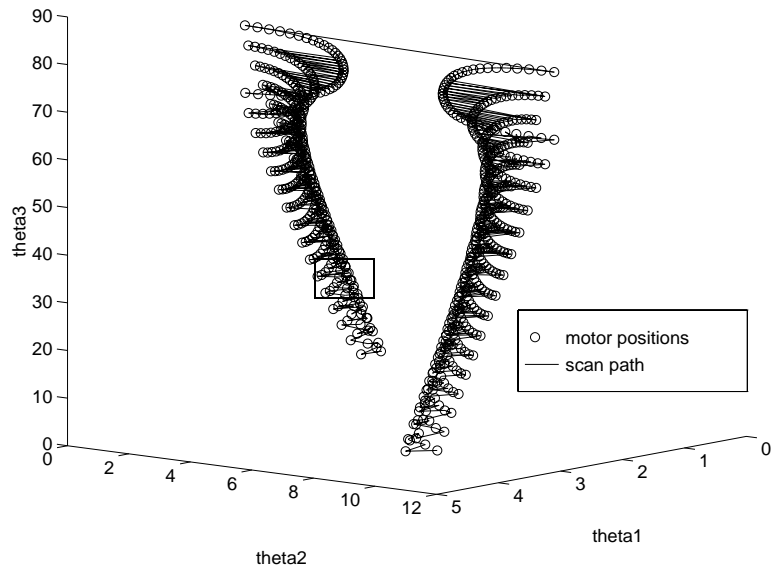


Figure 3.5: Optimized scan path, in solid line, shows the sequence to scan all the pre-determined measurement positions in θ_1 , θ_2 , and θ_3 . The three axes are scaled by the individual speeds of the motors to show the travel-time difference among the positions.

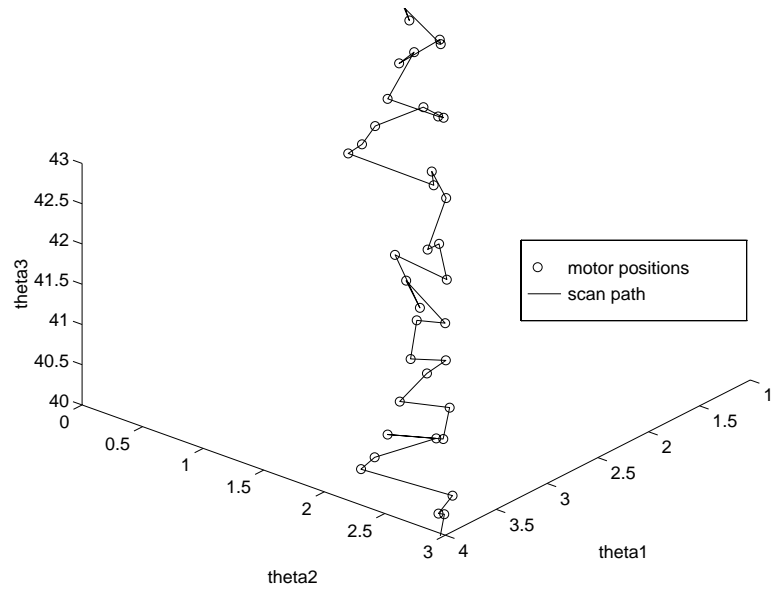


Figure 3.6: A magnified version of the box in Figure 3.5 showing the motors' positions and the scan path. The scan path in solid line represents the "traveling salesman's journey".

Chapter 4

Source and Viewing Optical Considerations and Design

In this chapter, we discuss the optical requirements for making BRDF measurements, before proceeding to discuss the specific designs of our light source and detector in later chapters. The optical approach and design considerations for our system are presented.

4.1 Defining the Reflecting-Surface Area

The exact portion of the test sample's surface entering the measurement of BRDF is to be carefully defined. We will call this area ΔA_r . It is the area which is entirely illuminated by the light source. The reflected light from this area is captured by the detector for BRDF calculation. Depending on how it is defined, ΔA_r can vary with either the incidence angle or with the view angle.

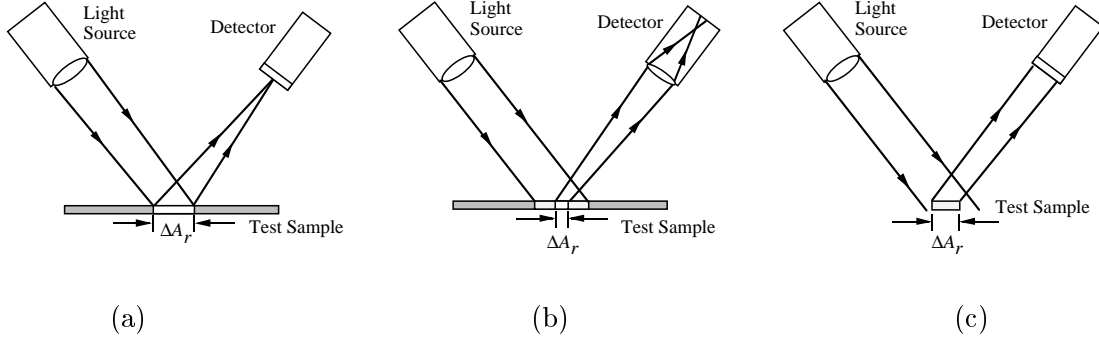


Figure 4.1: Three ways of defining the reflecting surface, ΔA_r .

A thorough discussion of possible source and detector optical configurations to define the reflecting surface area is given by Nicodemus *et al.* in [23]. ΔA_r can be defined by one of the following three methods:

1. Focus the irradiating beam onto the sample or onto the detector, and have the detector's field-of-view (FOV) cover the entire illuminated area. In this case, the entire illuminated area is the reflecting area, ΔA_r , which will be affected by the incidence angle of the source.
2. Use a sharply focused collecting beam. The detector optics focuses the test sample onto the detector head. ΔA_r is thus defined by the area of the magnified area of detector head projected onto the sample. It is important that the irradiated area is, at all times, large enough to encompass ΔA_r (where the focused collecting beam received reflected radiation), even at the largest obliquity.
3. Set the exposed area of the reflecting material itself as the reflecting area. The

irradiating beam and the detector’s field of view (FOV) must always cover the exposed area. ΔA_r is thus constant from all view directions.

There are practical difficulties with each of the methods above. Method 3 is the most difficult since it is difficult to avoid sensing the scattered stray light from the baffle, support, housing, or the edge of the sample.

A design similar to method 1 is discussed in [8], recommended by the American Society of Testing And Material (ASTM), and used by Stover [28]. In the design, a converging source beam is sharply focused on the detector’s collecting aperture. Method 2 is employed for our gonireflectometer. We prefer a detector that closely resembles a camera or an eye that would measure absolute radiance, just like the virtual camera in rendering scenes in computer graphics. We allow the reflecting area to scale according to the reciprocal of the cosine of the view angle, while maintaining a constant projected area in the view direction. When viewing at a large grazing angle, the detector reflectance is the average over a larger, skewed, object area.

Our system differs from the system recommended by ASTM and Stover (method 1) in the cosine factor appearing in the calculation of BRDF. Our measured data contains a $(\cos \theta_i)^{-1}$ factor, while if method one is employed, there will be a $(\cos \theta_d)^{-1}$ dependence instead. In other words, the reflecting area ΔA_r in our system is defined by the detector, whereas ΔA_r is defined by the source beam using method 1.

4.2 Calibration and Normalization

The conversion of the measured scattered power to a BRDF value involves normalizing the scattered power to the incident power, using either comparison or absolute measurements methods.. When using the comparison method, a sample with known BRDF, or known directional-hemispherical reflectance is used as a reference. The reference sample is first measured (at the known BRDF geometry, or integrated over the hemisphere), then the calibration factor to convert the measured power to a BRDF value is calculated. We use a Spectralon reference sample. Spectralon is a pressed PTFE (polytetrafluoroethylene) manufactured by Labsphere. PTFE is a material that is highly diffuse and spectrally flat in reflectance and widely used as reference for BRDF measurement [4] [9].

The absolute calibration method requires a direct measurement of the incident power. The method requires an optical configuration that allows direct measurement of the incident irradiance. This method works well for materials with reflectances ranging from Lambertian to highly specular. If the detector is incapable of measuring the direct irradiation due to saturation, neutral density filters with known transmittances can be used to attenuate the source power without upsetting the optical geometry.

For the irradiation measurement, the total illumination flux that would impinge on $\Delta A_r(\hat{s}_r)$ must be within the FOV of the detector and must be collected by detector solid angle $\Delta\Omega_d$ when the detector is looking directly at the source in the absence of a test sample. Even when a reference calibration/normalization is

employed, such optical configuration is necessary. The comparison method, using a diffuse reference sample with known reflectance, can usually achieve the same calibration factor as with the absolute calibration method. However, specular light reflected off ΔA_r can be missed by the detector if it is incapable of capturing the direct irradiance on ΔA_r .

In short, whichever calibration method is used, one should be able to compute a specular reflectance from a measured specular-direction BRDF by multiplying the measured BRDF by the the solid angle of the detector. This is not guaranteed by the mere ability of a gonioreflectometer to measure specular reflectance by taking the ratio of the measurement in the specular direction to the direct source measurement.

4.3 Requirements for the Light Source

Below are some considerations we made while designing a light source:

1. A uniform illumination across the entire illuminated area (of which the reflecting area $\Delta A_r(\hat{s}_r)$ is a subset) is required.
2. A small solid angle of illumination across the illuminated area is desirable. Parallel uniform light will be ideal but will require a very small (point-like) source. Condensing a tiny source to produce a collimated beam does not warrant radial uniformity.
3. The illumination angle of the rays within the beam that impinge on the reflecting area $\Delta A_r(\hat{s}_r)$ should be constant.

4. The source is required to be spectrally and radiometrically stable over the entire duration of measurement.
5. Using a focusing lens with minimal aberration to image a uniformly emitting source onto the sample will provide a uniform illumination. If the source is far enough from the target, the consistency of a solid angle of illumination is approximately maintained within the illuminated area.
6. The imaging of a uniformly emitting source onto the target has to be such that the defocusing of the image on a sample tilted from the image plane would still maintain an acceptable uniformity.
7. The rays within the beam of an “extended” source that are focused onto the target will diverge beyond the target. And an extended source focused at infinity will not give a uniform illumination in the target at a finite, small distance. If the magnification of the finite source is > 1 , the beam will be diverging despite the convergence of the rays onto the image plane.
8. The total illumination flux that would impinge on the reflecting area $\Delta A_r(\hat{s}_r)$, should be collected within the detector’s solid angle, $\Delta\Omega_d$, when the detector is looking directly at the source in the absence of a test sample. This is a required condition for absolute measurement calibration.
9. The source should be fully unpolarized or fully polarized. Tungsten lamps are usually partially polarized. Figure 4.2 shows the polarization bias of a typical coiled filament tungsten light bulb.

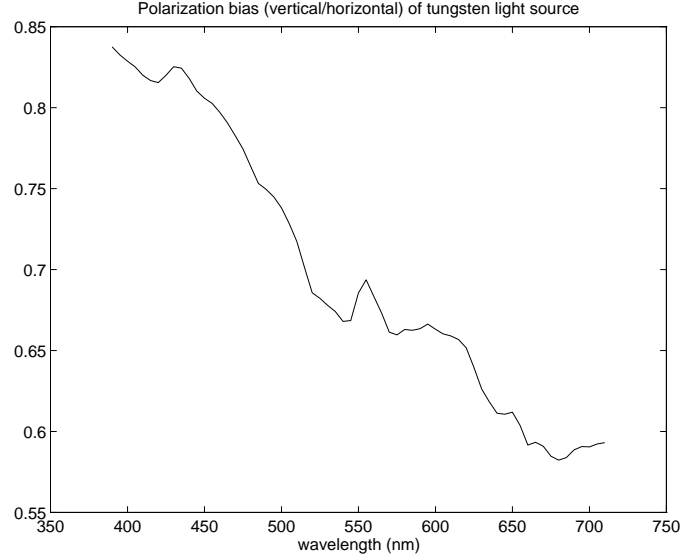


Figure 4.2: Spectral polarization bias of an HLX single coiled filament light source.

4.4 Detection of Reflected Radiance

The reflecting area, ΔA_r , needs to be determined carefully. The measured BRDF will be the average effect of the entire reflecting area. Choice of ΔA_r depends on roughness, or the size or the micro-scale structures of the material. For example, a piece of fabric, on a milliscale, has a rough woven structure. To measure the average BRDF of the fabric's surface, a reflecting area should cover sufficient samples of the woven structure that contribute to the overall far field reflectance pattern. Bartell *et al.* suggest that at least 100 of these surface elements be included in the sample (reflecting) area [1].

The polarization of the reflected light from a surface varies in different reflection directions which may affect the consistency of the detector's response; an auxiliary

apparatus such as an integrating sphere can be used as a receptor to depolarize the received radiation. The integrating sphere is also a good receptor to eliminate spatial inconsistency of the detector head [15] [21]. The directional reflected light is diffused by the integrating sphere. However, there is disadvantage to using an integrating sphere: The detection throughput is significantly lowered, especially when a spectrographic measurement is involved.

Using a focused collecting beam to define the reflecting-surface area gives us more control over what and how much we want the detector to “see.” A well-designed zoom lens can be used with the detector to allow measurements of variable ΔA_r , provided the test sample and the source beam are sufficiently large to avoid vignetting. The reflecting area $\Delta A_r(\hat{s}_r)$, which is the area on the sample whose reflected radiance will be detected by the detector, can be defined as follows:

$$\Delta A_{r0} = \Delta A_r(\hat{n}_r) = ml \times mw$$

$$\Delta A_r(\hat{s}_r) = \frac{\Delta A_{r0}}{\cos(\theta'_r)}$$

where l and w are the length and the width of the detector entrance slit, respectively; m is the magnification; and the view distance d_r determines the focal length of the focusing optics, or vice versa.

Since all of the energy $\Delta q_r(\hat{s}_r)$, reflected from $\Delta A_r(\hat{s}_r)$ in direction \hat{s}_r , is collected by the detector, the detector signal, V , is

$$V(\hat{s}_r) \propto \Delta q_r(\hat{s}_r)$$

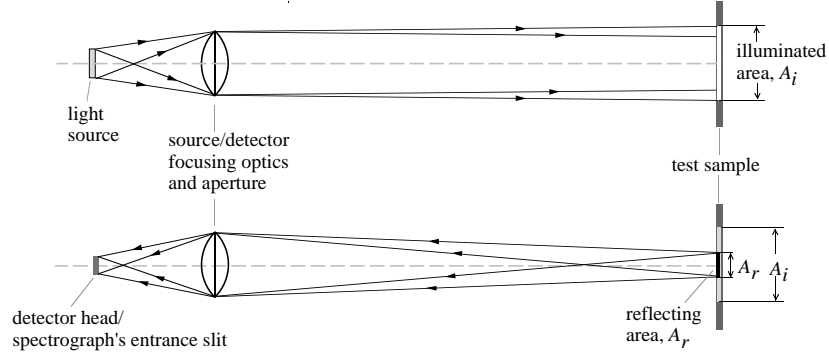


Figure 4.3: Optical configurations of illumination and radiance detection.

And, since the acceptance solid angle is fixed, the projected area of $\Delta A_r(\hat{s}_r)$ in \hat{s}_r direction is simply ΔA_{r0} . Hence, the detector signal is proportional to the viewed radiance, $L(\hat{s}_r)$:

$$\begin{aligned} \therefore \Delta q_r(\hat{s}_r) &\propto \Delta L(\hat{s}_r) \Delta A_{r0} \Delta \omega_r \\ \therefore V(\hat{s}_r) &\propto \Delta L(\hat{s}_r) \end{aligned}$$

Figure 4.3 shows the optical configurations of illumination and radiance detection for our system. The light source is focused at infinity to create a parallel beam of rays. The detector is focused on the test sample to define the reflecting surface area.

4.4.1 Size of Test Sample

Our receptor optics (a mirror tilted at 45°), placed at 26in. away, subtends an angle of 3° from the center of the sample. We allow a 2° tolerance and assume that the

largest view angle the detector is capable of reaching is 85° .

Thus, the magnification of the sheared reflecting area by the detector, going from the normal to the largest (closest to the surface) grazing angle (85°), is $11.5\times$.

$$\frac{1}{\cos(85^\circ)} = 11.5$$

The normally illuminated area on the test sample must also be at least 11.5 times the area viewed by the detector from the normal.

Having the detector view the sample through a folding mirror (45°) at a distance helps to prevent the source beam (which has a considerable diameter) from hitting the detector directly at large source-view angles.

4.5 Polarization Biases of Source and Detector

The polarization bias of the light source is defined as the ratio between the intensities of s polarized light component of the light emitted from the source, to that of the p polarized light component. The *polarization bias constant* of the detector is defined as the ratio of the detector spectral responses to two separate, equal intensity, incident light beams of different polarizations, i.e. the s polarization and p polarization, respectively.

In our gonireflectometer setup the source is rotated about the vertical axis while the detector is always held stationary, and the sample is rotated in two degrees of freedom. Thus, the polarization biases of both the light source and the detector viewed by the test sample vary in the sample coordinate as the sample is rotated. For

convenience, we redefine the polarization bias by replacing the s and p polarizations with v (vertical with respect to the lab frame) and h (horizontal with respect to the lab frame), respectively.

The polarization bias of the detector can be determined experimentally by having the detector measure, through a perfect polarizer, the light emitted from an integrating sphere source. Since the light emitted from an integrating sphere is highly unpolarized, the light that the detector measures for two perpendicular polarizer settings will be polarized light of equal intensities. If V_{0v} and V_{0h} are the signals corresponding to v and h polarized light, the v - h polarization bias of the detector, D_{vh} , is:

$$D_{vh} = \frac{V_{0v}}{V_{0h}}$$

A signal V_v from v polarized light is multiplied by D_{vh} so that it becomes a signal produced by the detector with a response curve identical to the detector's response to h polarized light. Clarke *et al.* [4] give a general discussion of polarization biases in goniophotometric measurement when both the light source and the detector are polarized.

Ideally a polarizer allows the light component of only one kind of polarization (whose electric field is parallel to the polarizer's pass axis) to pass through. Light with polarization perpendicular to the pass axis will either be completely absorbed or reflected. In reality, for a dichroic polarizer (we use Melles Griot 03FPG007), a small amount of the perpendicular component leaks through.

The total transmittance of the polarizer for a polarized light, polarized at an

angle θ from the pass axis, is:

$$\begin{aligned} P_{total} &= P_v(\theta) + P_h(\theta) \\ &= K_{v0} \cos^2 \theta + K_{h0} \sin^2 \theta \end{aligned}$$

where $P_v(\theta)$ and $P_h(\theta)$ are the power transmittances of the polarizer for v and h polarized light, respectively, and K_{v0} and K_{h0} are the transmittances at $\theta = 0^\circ$.

For simplicity, we will assume that $K_{h0} = 0$, and thus $P_h(0^\circ) = 0$, and $P_v(90^\circ) = 0$. If necessary, K_{v0} , K_{h0} as a function of wavelength can be found experimentally.

Chapter 5

The Light Source

The design, performance tests, and specifications of the light source used for the gonioreflectometer are described in this chapter. The light source is designed with the following *a priori* requirements:

1. spectrally continuous from near UV - VIS - NIR
2. spectrally and radiometrically stable over time
3. unpolarized
4. uniform across its beam
5. parallel ray

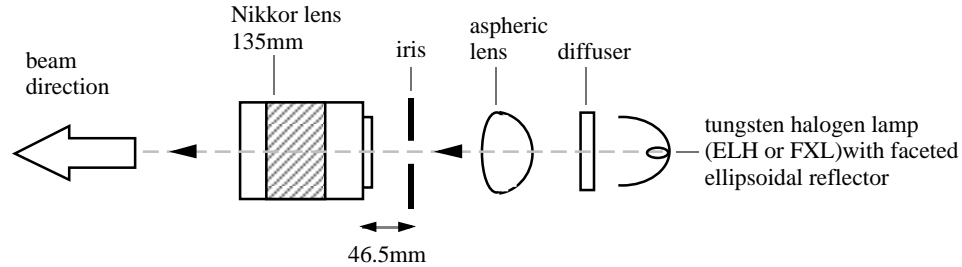


Figure 5.1: Schematic of the light source assembly.

5.1 Design And Components

Figure 5.1 shows the schematic of the light source. First, a broad band light with continuous spectrum is emitted from a tungsten halogen lamp with a multi-faceted ellipsoidal reflector (ANSII ELH, 300 W, or FXL, 410 W)¹ onto a flashed opal glass diffuser². The latter is a depolarizer ($> 96\%$). The depolarized light scattered from the diffuser is collected by an aspheric lens which in turn focuses the light onto an iris-aperture (a spatial filter). Within the narrow distance, an aspheric lens can collect more light than a convex lens, and do so at a lower F-number. A photographic lens (Nikkor 135mm), focused at infinity, is used to condense the light from the aperture.

The iris is stopped down to the smallest possible size that would still provide sufficient source throughput and the required beam size on the test target. A beam

¹Both the ELH and FXL have a double coiled (coil of a coil) filament, which should emit a less polarized light than a single-coiled filament.

²We use an Oriel 48020.

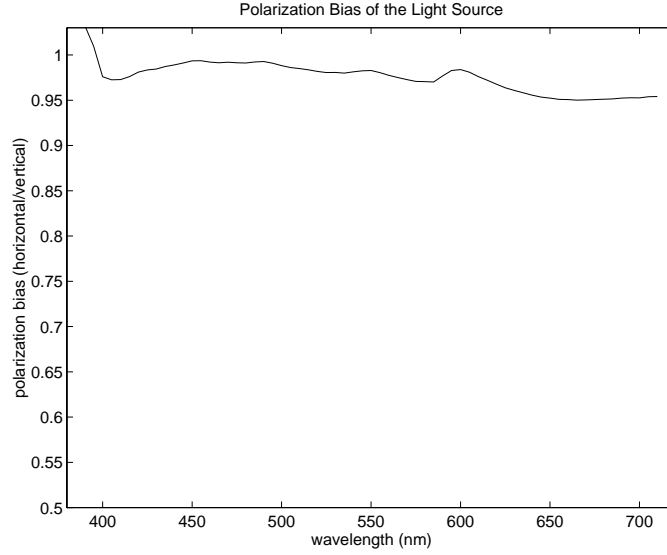


Figure 5.2: Polarization bias of the light from the source assembly.

of 6.5cm diameter is sufficient to cover the largest possible reflecting area (projected image of the detector slit that is maximally skewed at the largest obliquity on the sample). This upper bound beam diameter is estimated from:

$$D_{max} = \text{width of reflecting area, } A_{r0} \times \frac{1}{\cos 85^\circ \cos 45^\circ}$$

Here, we have assumed that the largest possible view angle is 85° and that the tilting of Stage 2 will lead to a $1/\cos 45^\circ$ skewed magnification.

The finite source-aperture causes spatial broadening of the beam. Assuming that the Nikon lens has minimal aberration, a perfectly parallel beam is possible only with an aperture of infinitesimal size. The polarization bias of the light source assembly is shown in Figure 5.2.

5.2 Uniformity

Figure 5.3 (a) shows the measured uniformity for the source beam. The beam was focused directly onto the detector and measurements were made on various locations of the beam. Figure 5.3 (b) shows the approximate locations where the measurements are taken. The curves “E_e” and “W_e” are samples very near the edge of the beam, and hence their intensities drop off significantly from the intensity at the center. Overall, the uniformity in the center region is above 90%.

5.3 Reciprocity

Some measurements were carried out to test if the system obeys reciprocity.

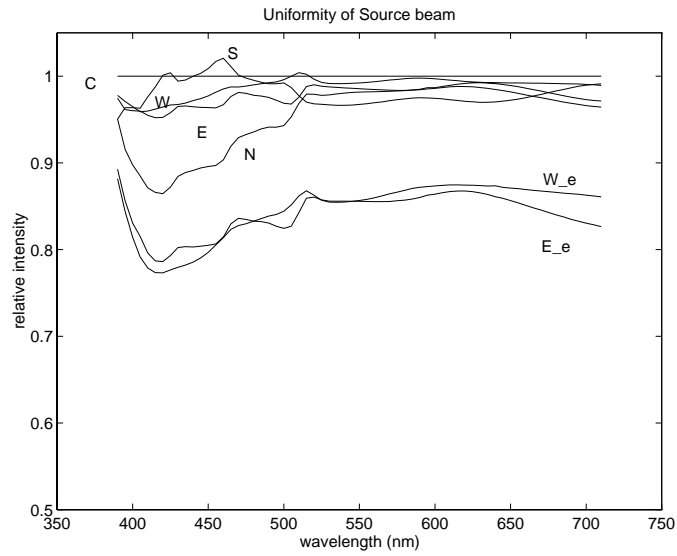
$$f_r(\hat{s}_i, \hat{s}_r) = f_r(\hat{s}_r, \hat{s}_i)$$

The measured signal $V(\hat{s}_i, \hat{s}_r)$ multiplied by the $\cos \theta_i$ is observed to remain constant when the source and the view directions are reversed. When the incidence and view angles measured from the normal are very far apart, for example, $[\theta_i = 5^\circ, \varphi_i = 0^\circ]$ and $[\theta_i = 85^\circ, \varphi_i = 0^\circ]$, the error in reciprocity increases.

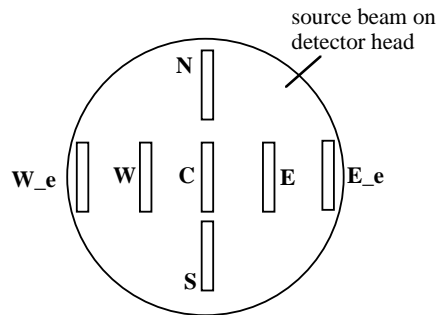
The results of the reciprocity test using a Spectralon sample and examples reciprocal BRDF measurements are given in Appendix E.

5.4 Stability

According to the manufacturer’s specification, the power supply for the light source (HP 6030A Autoranging System DC Power Supply) has a drift (stability) of 0.03%+5mA



(a)



(b)

Figure 5.3: (a) Measurements of source intensity at various positions (shown in (b)) across the source beam. The detector is focused at the test sample plane. All the measurements are normalized to the intensity reading at the center of the beam (location C). (b) Locations on the cross-section of the beam where measurements in (a) were made.

over an 8-hour interval under constant line load and ambient following a 30-minute warm up.

From monitoring the radiometric spectrum of the light source by the detector, we estimate the incident power shift to be approximately 4.5%.

Rated lifetime of the ELH lamp by the manufacturer is 35 hours. The FXL has a 50-hour lifetime. We recommend that the last 5 hours of their lifetime not be used in measurement, as a spectral shift could possibly have occurred, as observed in experiments.

Chapter 6

The Detector

In this chapter, we discuss the optical configuration and the performance of the detector for the gonireflectometer. We also discuss how an output signal from the detector is processed.

6.1 Design

The detector views the test sample through a folding mirror at a 90° angle, as shown in Figure 2.3. The folding mirror is placed at 45° with respect to both the detector and the test sample. This helps to prevent the large-size source beam from hitting the detector directly at a large source-view angles. The distance between the folding mirror and the test sample is 26 inches.

The entire detector assembly consists of a spectroradiometer (a spectrograph with a diode array detector) and auxiliary focusing optics that focus the reflected light from the sample, through the folding mirror, onto the entrance slit of the

spectrograph. The entrance aperture of the the focusing optics defines the receptor solid. A dichroic polarizer is placed in front of the focusing lens. Figure 6.1 shows the schematic of the detector assembly with its focusing optics.

6.1.1 The Oriel Multispec/Instaspec II Spectroradiometer

The Oriel Multispec/Instaspec II Spectroradiometer consists of two major components: a spectrograph and a 1024-pixel diode array detector. The spectrograph has a crossed Czerny-Turner design¹, with two focusing mirrors and a reflective interference grating of 600 lines/mm. The grating is matched to the 1024 array diodes to cover a readout spectrum spanning the visible range.

The minimum exposure time is 20ms (which corresponds to 1 detector exposure unit), with a read-time (the time taken to read the data from the photodiode array elements) of 13.6ms. There is a blanking period between each read-time used for computer overhead. The diode array detector is thermoelectrically cooled and has a 16-bit readout signal resolution. We will discuss the effective dynamic range of the detector in Section 6.5.2. We have chosen the operating temperature to be 15°C to match the ambient temperature and the humidity in the laboratory. Operating the detector at a lower temperature will risk the detector being damaged by water vapor condensation. The temperature in the laboratory is always maintained at a specific temperature, between $\sim 64^{\circ}F - 70^{\circ}F$.

The size of the detector's entrance slit is .280mm \times 2mm. This size is chosen

¹A form of monochromator optical system consisting of two spherical mirrors used in conjunction with a movable diffraction grating or prism [16].

to give maximum throughput and yet a normal reflecting area of favorable size on the test sample. The normal reflecting area, ΔA_{r0} , is equal to the product of the magnification of the focusing optics and the slit size.

6.1.2 Focusing Optics

An achromatic doublet is used in conjunction with a companion aplanatic meniscus to focus the illuminated area of the test sample onto the detector's entrance slit. The aplanatic meniscus is used to shorten the focal length of the doublet and reduce the F-number without decreasing the doublet's performance. The doublet has a paraxial focal length of 120.0mm, a diameter of 40.0mm, and a thickness of 11.2mm along the principal axis. The meniscus has a paraxial focal length of 175.2mm, a diameter of 40.0mm, and a thickness of 7.0mm along the principal axis.

The doublet and the meniscus are spaced 1mm apart and are oriented with the concave surface of the meniscus towards the focal point. This is near where the entrance slit of the detector lies. The lens combination gives a front focal length of 59.9mm, measured from the concave surface of the meniscus to the focal point. The F-number of the combination is 1.78.

The magnification of the lenses is approximately $11\times$. The entrance slit is $0.280\text{mm} \times 2\text{mm}$ in dimension, resulting in the normal projected reflecting area, A_{r0} , on the sample of size $\sim 3.08\text{mm} \times 22\text{mm}$.

The receptor solid angle is estimated from the ratio of the exposed doublet area and the square distance from the doublet (via the folding mirror) to the sample. Since the square folding mirror ($50\text{mm} \times 50\text{mm}$) is placed at 45° with respect to

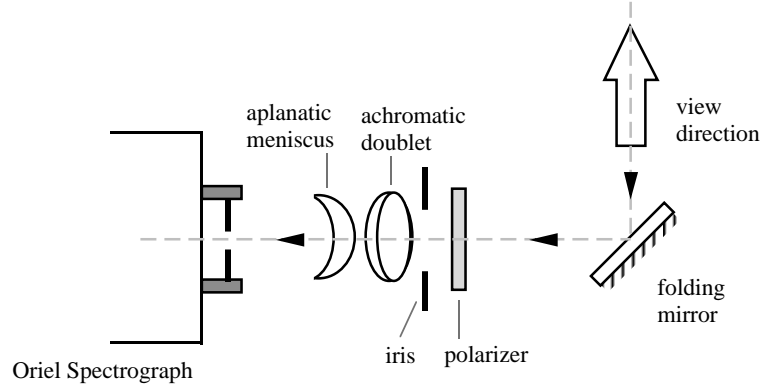


Figure 6.1: Schematic of the detector's focusing optics.

the detector, its projected area becomes $35\text{mm} \times 50\text{mm}$. There is a 0.75% area of the doublet (dia. = 40mm) that is clipped on the two sides by the mirror. The distance from the sample to the folding mirror is 26in. and the distance from the folding mirror to the doublet is 6.5in. Theoretically, if the entire exposed area of the doublet is the effective receptor, the receptor solid angle would be

$$\begin{aligned}\Omega_d &= \frac{0.9925(1.83\text{cm})^2\pi}{(26\text{in.} + 6.5\text{in.})^2} \\ &= 0.00153\text{sr}\end{aligned}$$

From experiments involving measuring the reflectance of a Spectralon, a white reference sample, we approximated that the effective solid angle of the detector should be 0.0028sr. This means that effectively 83.6% of the doublet's front exposed area is receiving light.

6.2 Spectral Calibration

The focusing mirrors in the spectrograph have a flat field focus on the diodes and reflect the diffracted incoming light onto the diode array. The pixel numbers thus vary linearly with wavelength. Assuming that the incident light beam on the diffraction grating is unidirectional, we can easily justify the use of the linear model from the grating formula, $d \sin(\theta_i) + d \sin(\theta_r) = m\lambda$, where d is the separation between two grooves on the grating, θ_i is the incidence angle, θ_r is the diffraction angle, m is the order of diffraction, and λ is the wavelength. Using a blocking filter to avoid overlapped spectra from different orders of diffraction is not necessary in this setup. The wavelength range in which we are interested is between 390nm to 710nm and the intensity of the source's ultraviolet radiation below 390nm is negligible. 390nm times 2 is 780nm, so a blocking filter is not required in the region between 390nm to 710nm.

The Optronic OL750-M monochromator and a red HeNe laser (632.8nm) were used to calibrate the grating position. The monochromatic source emitted from the OL750-M was focused onto the Multispec Spectrograph entrance slit. The detector was placed 6 feet away from the monochromator. The monochromator and the focusing optics were aligned in a straight line to ensure that the optical calibration was done for light normally incident on the entrance of the detector. By adjusting the micrometer on the Multispec Spectrograph, the grating was adjusted such that 550nm wavelength was situated in the middle of the diode array at pixel number 511. The monochromatic source was stepped from 400nm to 725nm, at intervals of

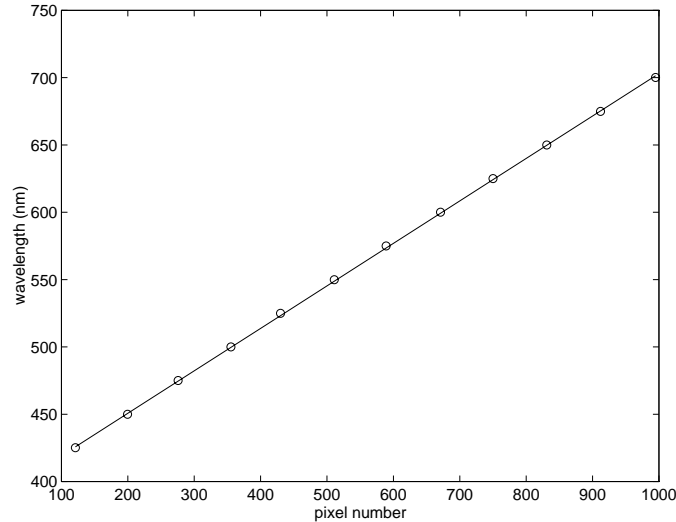


Figure 6.2: Plot of recorded points and fitted straight line for the array-diode wavelength calibration.

25nm, and the pixel number corresponding to each wavelength was recorded. The final micrometer reading was 2.735 (micrometer units).

A straight line, $y = ax + b$, was least-square fitted through the recorded points, where $y = \text{wavelength (nm)}$, and $x = \text{pixel number}$ ². See Figure 6.2.

6.2.1 Spectral Resolution and Signal Noise

From the spectral calibration discussed in the preceding section, the shortest wavelength (pixel 0) is 386nm, and the longest wavelength (pixel 1023) is 711nm, which corresponds to a spectral resolution of 0.32nm/pixel. The effective resolution of the signals, taking into account the various spectral broadening, is $\delta\lambda = 2.8\text{nm}$.

²The values are $a = 0.3154$ and $b = 387.6032$.

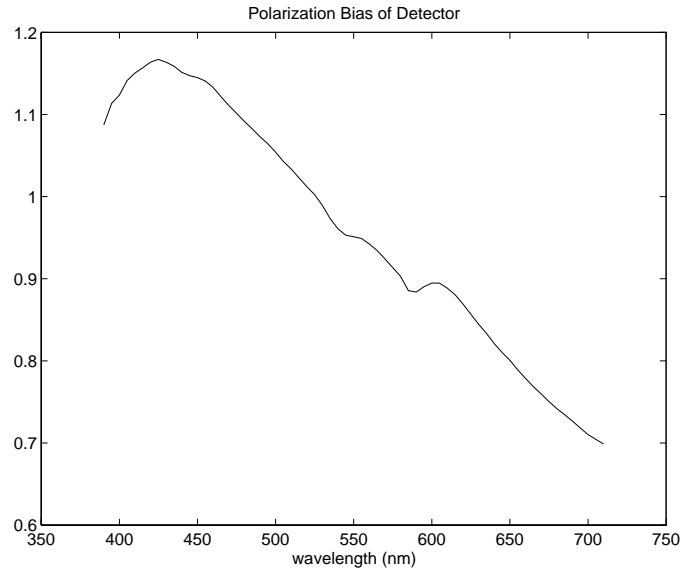


Figure 6.3: Polarization bias of the detector.

6.3 Polarization Bias

Chiefly due to the diffraction grating, the detector exhibits a polarization bias. It responds differently to incident light of different polarizations. The polarization bias of the detector was obtained by placing a polarizer in front of the detector and taking the ratio of two measurements of two perpendicular polarizer settings with the detector focused at the port of an illuminated integrating sphere. An integrating sphere is a good depolarizer.

We have measured the transmittance of a pair of crossed polarizers and have found that with the light source we use, the measured signals were comparable to the detector noise. Figure 6.3 shows the spectral polarization bias of the detector.

6.4 Radiometric calibration

We have experimentally verified that the detector responds linearly to the change in exposure time and integration time, for exposure of $3 \times 20\text{ms}$ to $1000 \times 20\text{ms}$. The radiometric linearity of the detector has been experimentally verified using neutral density filters at a fixed exposure time.

6.5 Signal Processing

6.5.1 Detector Noise

The total random noise in the measured signal consists of *dark current*, *photon noise*, and *electronic* or *amplifier noise*. Dark current is the thermal noise which increases as a function of temperature and time. Photonic noise, or *photon shot noise*, is proportional to the square root of the collected signal. The photonic noise has an zero expectation value and, with sufficient samples, can be averaged out.

Our detector sensor head consists of an array diode of size 1024 and is capable of capturing the diffracted spectrum from 386nm to 711nm. 1024 samples is excessive. To smooth/average and down-sample the signal, the 1024 samples are convolved with a smoothing filter of size 11 and then decimated to 65 samples that span the wavelengths from 390nm to 710nm at intervals of 5nm. The spectral resolution of the 1024 fine sampling is 0.32nm/pixel, with an effective spectral resolution of 2.8nm. Convolution with our size 11 smoothing filter effectively performs a weighted binning of the samples. The binning process, similar to integrating, averages the

signals, reduces the random noise, and minimizes noise with zero expectation value.

For the smoothing process, we chose to use a truncated Gaussian filter, as shown in Figure 6.4. The Gaussian filter has a size of 11, with $\sigma = 2.0nm$. The smoothing process results in a final signal with wavelength resolution of approximately 5nm, which happens to be the wavelength interval of the resultant signal.

The spectral broadening of the original signal ($\delta\lambda = 2.8nm$) is roughly a Gaussian, and after the convolving with a Gaussian filter, the resultant signal should remain Gaussian broadened.

We model the detector noise as

$$n_{total} = n_t t + n_{floor} + n_{random}$$

where n_{floor} is the noise offset constituting mainly amplifier noise, and n_t represents the noise which increases linearly in time. Both n_{total} and n_{floor} are constants. n_{random} is the random noise which represents the fluctuation of the signal, and has zero expectation value. A non-linear term can be added if the required exposure exceeds 20s.

The linearity of $n_t t + n_{floor}$ has been proven experimentally for exposure time ranging from 20ms to $1000 \times 20ms$. This portion of the noise can be characterized. The detector sampling interval is 20ms.

Observed standard deviations of the random noise signals are

$$\sigma(t = 20ms) = 2.46\text{counts/s}$$

$$\sigma(t = 3ms) = 0.8\text{counts/s}$$

$$\sigma(t = 500 \times 20ms) = 0.0216\text{counts/s}$$

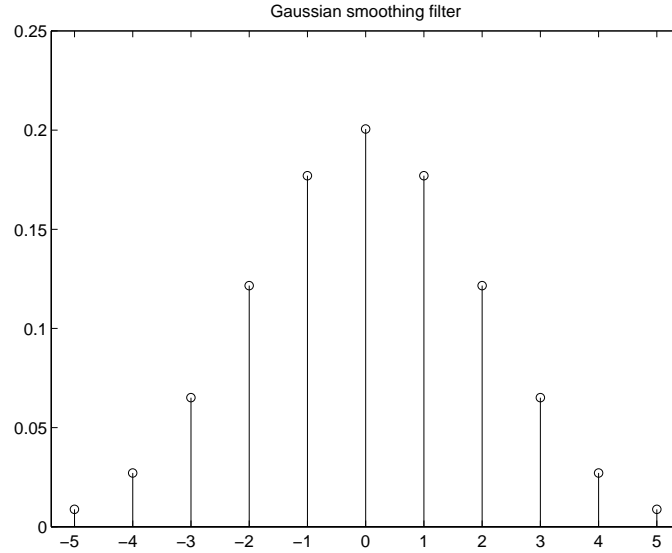


Figure 6.4: The Gaussian smoothing filter.

The variance of the random noise increases exponentially in time, but the signal count per unit time decreases as the exposure time is increased.

6.5.2 Dynamic Range

Regardless of the exposure time used, a signal is always normalized to a quantity V , in counts per unit time:

$$V = \frac{V_{raw} - n_{total}}{\text{exposure time} \times \text{number of integration}}$$

where V_{raw} is the measured raw signal. The total noise, n_{total} , can either be calculated from characterized noise parameters (n_t and n_{floor}), assuming that n_{random} is zero after the signal is smoothed, or obtained from direct measurement.

The Oriel spectroradiometer provides a 16-bit signal. For a fixed exposure time,

its dynamic range is approximately 1:20,000, according to the Oriel's specification. Since we have verified that within the exposure range in which we operate the detector, the response of the detector is linear with the exposure time and the noise level follows a linear model, we vary the exposure time to provide a reasonable signal-to-noise readout while avoiding signal clipping when the radiation is too strong.

In spite of the fixed detector dynamic range, when the exposure is varied according to signal strength, the acquired data achieve an effective dynamic range of approximately 1:380,000 using an ELH lamp, or 1:450,000 using an FXL lamp. The effective dynamic range is estimated by taking the ratio of the mean of the 100% direct source signal, across the entire spectrum, to the noise level (at 10s exposure) in signal counts per unit time.

Chapter 7

Errors

This chapter provides a quick examination of the deterministic errors in BRDF measurements taken using our system. *Deterministic* errors are errors that can be estimated from measurement uncertainties. *Systematic*, or system level, errors arise as errors in the proposed measurement *system*, or *concept*. These are estimated in Chapter 9 by comparing our measurements against other measurements in our laboratory or against reference materials. Most of the contributing errors in the various parameters that went into the derivation of the BRDF are estimated and deduced from experiments. The overall error estimation presented here is not the precise error of the instrument, but a rough estimate of the major source of errors affecting the BRDF measurement. Estimates of these errors provide an *a priori* knowledge of the accuracy of the measured data.

7.1 Sources of Errors

By using the absolute calibration method described in Chapter 8.2, we calculate measured BRDF as follows:

$$\begin{aligned} fr(\hat{s}_i, \hat{s}_r) &= \frac{K_\lambda V_r(\hat{s}_i, \hat{s}_r)}{\cos \theta_i} \\ &= \frac{V_r(\hat{s}_i, \hat{s}_r)}{V_0 \Delta \Omega_d \cos \theta_i} \end{aligned}$$

where

$$V_0 = V_r(\hat{n}, -\hat{n})$$

is the measured signal (in signal counts/unit time) of the direct source with the detector looking at the source in the absence of a test sample.

Fractional error of the measured BRDF is

$$\frac{\delta fr}{fr} = \left\{ \left(\frac{\delta V_r}{V_r} \right)^2 + \left(\frac{\delta V_0}{V_0} \right)^2 + \left(\frac{\delta \Delta \Omega_d}{\Delta \Omega_d} \right)^2 + \left(\frac{\delta \theta_i \cdot \sin \theta_i}{\cos^2 \theta_i} \right)^2 \right\}^{\frac{1}{2}}$$

The error in the computed BRDF increases dramatically as incidence angle becomes highly grazing. Figure 7.1 shows the percentage error of the measured BRDF as a function of wavelength. At $\theta_i = 85^\circ$, the error would have increased to 78%. In generating the overall error estimate shown in Figure 7.1, systematic error values of the parameters were taken into account. The deduction of the individual parametric errors will be discussed in the following sections.

7.2 Measured Signal

The scattered power measurement error $\delta V_r/V_r$ encompasses the following errors [3]:

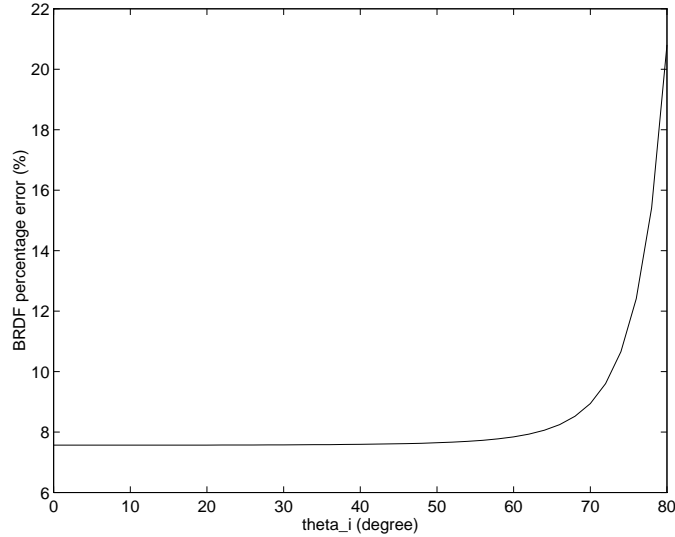


Figure 7.1: Estimated percentage error of BRDF measurement as a function of θ_i .

- receiver polarization misalignment
- aperture misalignment
- system noise
- detector non-linearity

By readjusting the polarizer multiple times, we observed from experiments that the receiver polarization misalignment error is less than $1e-4$. In the range of source strengths with which we deal, our detector is quite radiometrically linear. We estimate that, together, the aperture misalignment and hysteretic fluctuation of detector thermal control contribute to a typical maximum error of 0.5%, which is no larger than 1% across the entire spectrum. A large error here arises from the non-uniformity of the source beam.

What we refer to as a *signal*, be it the direct incident source measurement V_0 or a reflected radiance measurement V_r , is the radiometric quantity in signal counts per unit time. It is a result of subtracting noise from raw signals of specific polarizations, depolarization (if necessary), and normalization by exposure. There are numerous parameters that govern the accuracy of a signal. The detailed procedures used to obtain a noise-free, normalized, and unpolarized signal from the raw detector outputs are outlined in Appendix D. The incident power measurement error is similar to the scattered power measurement error with an additional error coming from source temporal error – in other words, the instability of the source. From observing the radiometric spectrum of the source over an 8 hour period, we estimate that the incident power measurement error ($\delta V_0/V_0$) is $\sim 4.5\%$ over the entire spectrum. Both the scatter power measurement error and incident power measurement error are functions of wavelength.

7.3 Noise Equivalent BRDF

A plot of the noise equivalent BRDF is shown in Figure 7.2, for $\theta_i = 0^\circ$ across the entire spectrum. This is a measured standard deviation of the random noise that has been converted to BRDF values. The dramatic increase in error towards the ultraviolet is not an attribute of the random noise, but a direct consequence of the errors that occur in the irradiance measurement, which was used in converting the random signals to BRDF values. This observed error trend will appear in measurements in a later chapter, and will be used to determine the operational

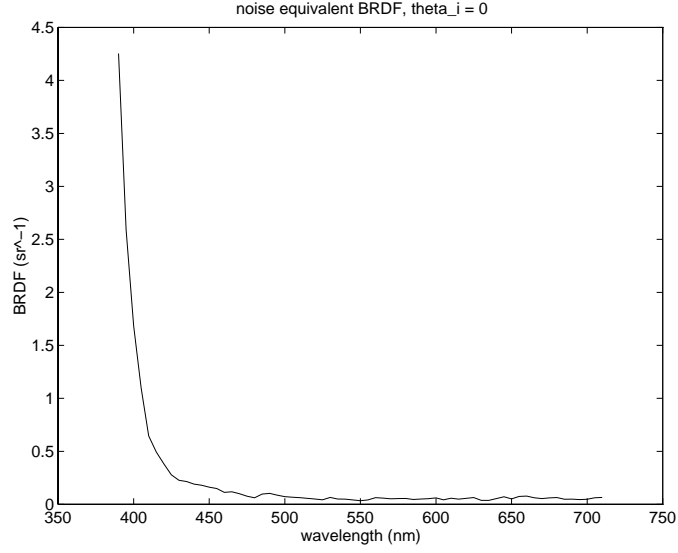


Figure 7.2: Noise equivalent BRDF, assuming $\theta_i = 0^\circ$.

spectral range of the reflectometer.

$$\text{Noise equivalent BRDF} = \frac{n_{\text{random}}}{V_0 \cdot \Omega_d \cdot \cos \theta_i}$$

7.4 Angular Accuracy

The solid angle of the detector is defined as follows:

$$\Delta\Omega_d = \frac{\Delta A_d}{l^2}$$

And the fractional error is

$$\frac{\delta\Delta\Omega_d}{\Delta\Omega_d} = \left\{ \left(\frac{\delta\Delta A_d}{\Delta A_d} \right)^2 + \left(\frac{\delta l}{l} \right)^2 \right\}^{\frac{1}{2}}$$

where l is the distance between the sample and the detector entrance aperture.

From measuring the BRDF of Spectralon and watching the change of the BRDF with the variation of the size of the solid angle, we estimated the $\delta\Delta\Omega_d/\Delta\Omega_d$ error to be around 6%.

The angular accuracy of our goniometric stages is estimated to be within 0.34° , which we determined by watching the deflected laser beam from a mirror sample at various motor positions during the alignment process.

It is difficult to quote the exact error of each BRDF measurement since the error is both spectroradiometric and opto-geometric. Hardware precision also plays an important factor in the accuracy of the measurement. The errors in our measurements are acceptable for the purpose of computer graphics rendering.

Chapter 8

Calibration and Normalization

We experimented with two types of calibration methods to convert a measured reflection to a BRDF value. The first method uses a reference sample with known directional-hemispherical reflectance. Measurements acquired over the entire hemisphere above the sample's surface are integrated, and the calibration factor is calculated. The second method, called an absolute method, does not employ a reference sample but has the detector view the light source directly in order to measure the total irradiance. The absolute calibration is preferred since it is relatively easy to perform and can be repeated for every set of new measurements.

8.1 Relative Calibration Using A Diffuse Standard Reference

Here we recapitulate the definition of the BRDF, $f_r(\hat{s}_i, \hat{s}_r)$:

$$f_r(\hat{s}_i, \hat{s}_r) = \frac{dL_r(\hat{s}_i, \hat{s}_r)}{dE_i(\hat{s}_i)}$$

For now, we will ignore the wavelength dependence and polarization in the BRDF. We add a subscript λ to both the calibration factors, K_λ , and C_λ , to indicate that calibration factors are computed for all wavelengths.

When a BRDF is measured with the gonioreflectometer, sampling is discrete and solid angles are finite. The illuminating light source is fixed and the total irradiation flux, E_i [w m⁻²] is confined to within the incident solid angle $\Delta\Omega_i$. $\Delta\Omega_i$ is equal to the source solid angle $\Delta\Omega_s$. Hence, $E_i \rightarrow \Delta E_i(\hat{s}_i)$ and $\Delta\Omega_i \rightarrow \Delta\Omega_s$.

$$\Delta E_i(\hat{s}_i) = \Delta E_0 \cos(\theta_i)$$

where ΔE_0 is the source irradiance at normal direction.

The measured signal V in the \hat{s}_r direction, is proportional to the reflected radiance $\Delta L_r(\hat{s}_i, \hat{s}_r)$, in \hat{s}_r . C_λ is the factor used to convert a measured signal to a real radiance value.

$$\Delta L_r(\hat{s}_i, \hat{s}_r) \propto V(\hat{s}_i)$$

$$\Delta L_r(\hat{s}_i, \hat{s}_r) = C_\lambda V(\hat{s}_i)$$

The measured BRDF at view direction \hat{s}_r and for illumination source from \hat{s}_i is therefore

$$\begin{aligned}
f_r(\hat{s}_i, \hat{s}_r) &= \frac{\Delta L_r(\hat{s}_i, \hat{s}_r)}{\Delta E_i(\hat{s}_i)} \\
&= \frac{C_\lambda V(\hat{s}_i, \hat{s}_r)}{\Delta E_0 \cos \theta_i} \\
f_r(\hat{s}_i, \hat{s}_r) &= \frac{K_\lambda V_r(\hat{s}_r)}{\cos \theta_i}
\end{aligned}$$

where

$$K_\lambda = \frac{C_\lambda}{\Delta E_0}$$

is the calibration factor, as a function of wavelength, needed to convert a measured signal to a BRDF value. To find K_λ , a Spectralon sample which has a known directional hemispherical reflectance at an incidence angle of 8° is used.

We know that the directional hemispherical reflectance at an incidence direction of $\hat{s}_i = \hat{s}_{i0}$ is

$$\rho_{dh}(\hat{s}_{i0}) = \int f_r(\hat{s}_{i0}, \hat{s}_r) \cos \theta'_r d\Omega_r$$

and the total reflected flux density is

$$\begin{aligned}
E_r &= \int L_r(\hat{s}_i, \hat{s}_r) \cos \theta'_r d\Omega_r \\
&= \int \int f_r(\hat{s}_i, \hat{s}_r) \cos \theta'_r L_i(\hat{s}_i) \cos \theta'_i d\Omega_i d\Omega_r \\
&= \int \int f_r(\hat{s}_i, \hat{s}_r) \cos \theta'_r dE_i d\Omega_r \\
&= \int \rho_{dh}(\hat{s}_i) dE_i
\end{aligned}$$

In our gonioreflectometer system, the incident irradiation is uni-directional; hence, this becomes

$$E_r = \rho_{dh}(\hat{s}_i) \Delta E_i(\hat{s}_i)$$

In the calibration process, the incident light is set at $\theta_{i0} = 8^\circ$, and we can measure E_r by integrating over the entire hemisphere above the Spectralon sample,

$$E_r = \sum_{hemi} \Delta L_r(\hat{s}_i) \cos \theta'_r \Delta \Omega_r$$

And combining the two equations above,

$$\begin{aligned} \Delta E_{i0}(\hat{s}_{i0}) &= \Delta E_0 \cos \theta_{i0} \\ &= \frac{1}{\rho_{dh}(\hat{s}_{i0})} \sum_{hemi} \Delta L_r(\hat{s}_r) \cos \theta_r \Delta \Omega_r \end{aligned}$$

The calibration factor K_λ can thus be calculated as shown below, where ρ_0 ($\rho_{dh}(\theta_i = 8^\circ)$) is the directional hemispherical diffuse reflectance of the Spectralon sample at $\theta_{i0} = 8^\circ$.

$$\begin{aligned} \frac{K_\lambda V_r(\hat{s}_r)}{\cos \theta_{i0}} &= \frac{\Delta L_r(\hat{s}_{i0}, \hat{s}_r)}{\Delta E_i(\hat{s}_{i0})} \\ &= \frac{\rho_0 C_\lambda V(\hat{s}_r)}{\sum_{hemi} \Delta L_r(\hat{s}_r) \cos \theta'_r \Delta \Omega_r} \\ &= \frac{\rho_0 C_\lambda V(\hat{s}_r)}{C_\lambda \sum_{hemi} V(\hat{s}_r) \cos \theta'_r \Delta \Omega_r} \end{aligned}$$

$$K_\lambda = \cos \theta_{i0} \cdot \frac{\rho_0}{\sum_{hemi} V(\hat{s}_r) \cos \theta'_r \Delta \Omega_r}$$

8.2 Absolute Calibration by Measuring The Direct Irradiance

The absolute calibration is carried out by having the detector view the light source directly. The optics of the source has to be such that when the detector is looking directly at the source, all of the source irradiating flux impinging on the reflecting area ΔA_{r0} , is captured by the detector, and other rays entering the detector's FOV will not be sensed by the detector's head (or the detector's entrance slit). Provided that the uniformity and the solid angle of the source beam across the reflecting area remains constant at all sample orientations, we will have an irradiating flux $dE_i(\hat{s}_i)$, that satisfies:

$$dE_i(\hat{s}_i) = dE_0 \cdot \cos \theta_i$$

where $dE_0 = dE_i(\hat{s}_i = \hat{n})$. The BRDF can be computed from the reflected signals and the direct illuminant signals, since the measured signal V is proportional to the energy flux Δq , which is also proportional to the reflected radiance:

$$\Delta L_i = \Delta q_i \cdot \Delta A_r^{-1} \cdot \Delta \Omega_i^{-1}$$

$$\Delta L_r = \Delta q_r \cdot \Delta A_r^{-1} \cdot \Delta \Omega_r^{-1}$$

$$\Delta V_r = C_\lambda \Delta q_r$$

The differential d is replaced by Δ for a measurement system to indicate finite quantities. The finite irradiating flux on ΔA_r becomes

$$\begin{aligned}\Delta E_i &= \Delta L_i \Delta \Omega_i \\ &= \Delta q_i \Delta A_r^{-1}\end{aligned}$$

$$\Delta E_0 = \Delta q_{i0} \cos \theta_i \Delta A_r^{-1}$$

$$\begin{aligned}f_r(\hat{s}_i, \hat{s}_r) &= \frac{dL_r(\lambda, \hat{s}_i, \hat{s}_r)}{dE_i(\hat{s}_i)} \\ &= \frac{dL_r(\hat{s}_i, \hat{s}_r)}{dE_0(\hat{n}) \cos(\theta_i)}\end{aligned}$$

$$\begin{aligned}f_r(\hat{s}_i, \hat{s}_r) &\approx \frac{\Delta L_r(\hat{s}_i, \hat{s}_r)}{\Delta E_i(\hat{s}_i)} \\ &= \frac{\Delta q_r \cdot \Delta \Omega_d^{-1} \cdot \Delta A_r^{-1}}{\Delta q_i \cdot \Delta A_r^{-1} \cos(\theta_i)} \\ &= \frac{K_\lambda V_r(\hat{s}_i, \hat{s}_r)}{\cos \theta_i}\end{aligned}$$

where $\Delta \Omega_d$ is the detector solid angle.

K can be found by measuring the direct illumination, viewing the light source directly at $\theta_i = 0^\circ$ and $\theta_r = 180^\circ$ in the absence of a test sample. The total irradiating flux, Δq_{i0} , falling on the sampled area ΔA_0 on the test sample, will be collected as the reflected flux Δq_r within the receptor solid angle $\Delta \Omega_r$.

$$\Delta q_r = \Delta q_{i0}$$

The calibration factor K_λ is calculated from the measured signal $V_r(0^\circ)$ of the direct illumination follows:

$$K_\lambda = V_r(0^\circ)^{-1} \cdot \Delta \Omega_d^{-1}$$

Chapter 9

Measurements and Results

Some measurement results are presented in this chapter. The following three kinds of reflectance measurements were made with the gonireflectometer:

1. specular reflectance

$$\rho_s = \frac{dL_r}{dL_i}$$

2. bidirectional reflectance (BRDF)

$$f_r = \frac{dL_r}{dE_i}$$

3. directional hemispherical reflectance

$$\rho_{dh} = \int f_r \cos \theta_r d\Omega_r$$

The first was obtained by taking the ratio of the reflected flux in the mirror direction to the direct irradiance. The second was obtained by both absolute and

relative methods, described in Chapter 8. The latter was obtained by integrating the measured BRDF values over the hemisphere.

For all measurements, the gonioreflectometer was first aligned optically by using the procedures in Appendix B. For absolute BRDF measurements, the measurement sequence is outlined in Appendix C. The procedures for processing the resulting signals are described in Appendix D.

In this chapter, we investigate the systematic measurement error by making measurements of the standard samples and instrument cross-checking. As an instrument cross-check, we compare the specular reflection measurements made with our gonioreflectometer to measurements of the same samples made with the Optronic Specular Reflectometer OL-740-75M¹. The comparisons of our measured BRDF of the Spectralon sample to measurements published by both the Rochester Institute of Technology [10] and Labsphere [27] are presented. We also compared the directional-hemispherical reflectance obtained with our system to measurements made with the Optronic Diffuse reflectometer OL 740-70.

From our measurements, we conclude that the spectral operational range for the instrument is from 420nm to 710 nm, although all the measurements are presented with measured wavelengths from 390nm to 710nm.

¹The Optronic OL-750 Spectroradiometer comprises the OL-740-75M Specular Reflectance Attachment and the OL-740-70 Diffuse Reflectance Attachment.

9.1 Instrument Signature

First, in Figure 9.1, we show what we call the *instrument signature*, which is measured by scanning the incident beam in the absence of a test sample (from $\theta_3 = 178^\circ$ to $\theta_3 = 182^\circ$). The total observed width of the signature is about 3° , with its half bandwidth smaller than 2° . Assuming that our light source is adjusted to emit very parallel light with negligible incidence solid angle, and the solid angle subtended by our detector head (the entrance slit of the detector) is also negligible, then we can attribute the broadening of the signature curve mainly to the finiteness of the detector entrance aperture – in our case, the size of the achromatic doublet. This effect is called *aperture convolution*, since the signature curve is a result of the aperture convolving with the source beam. The peak of the measurement corresponds to the reciprocal of the detector's solid angle, which is the upper limit of the BRDF measurement at $\theta_i = 0^\circ$. As the receiver solid angle approaches 0, the BRDF approaches infinity, which is equivalent to an ideal 100% specular reflection.

The effective width of the illumination beam of parallel rays seen by the detector is the size of the magnified detector slit on the sample plane. At a normal view direction, this is approximately $3.8\text{mm} \times .2\text{mm}$. The width of 3.8mm subtends a small angle of $.3^\circ$. The Gaussian-like drop off within the signature curve is caused by other factors: non-uniformity of source beam, lens aberrations, etc.

The measured BRDF ($\theta_i = 45^\circ$, $\lambda = 550\text{nm}$) of a vacuum coated first-surface aluminum mirror is shown in Figure 9.2. The spatial broadening of the curve is comparable to that of the in-plane instrument signature in Figure 9.1. The off-

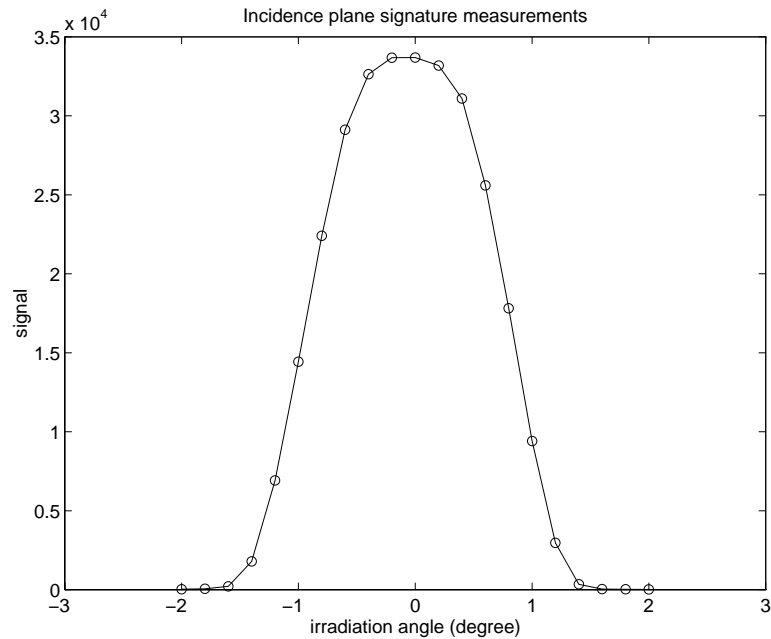


Figure 9.1: The signature is measured (at $\lambda = 650\text{nm}$) with the light source moving from $\theta_3 = 178^\circ$ to 182° , without a test sample. The broadened curve shows the effect of aperture convolution since the detector has a finite aperture and the reflecting area on the sample plane is finite.

centered peak observed is caused by slight misalignment of the sample on the sample holder.

9.2 Specular Reflectance

In this section, we examine the polarized specular reflection of two materials, measured with our gonioreflectometer. The two materials are a vacuum coated aluminum (on glass) mirror and a blue plastic lucite. When a polarized incident source

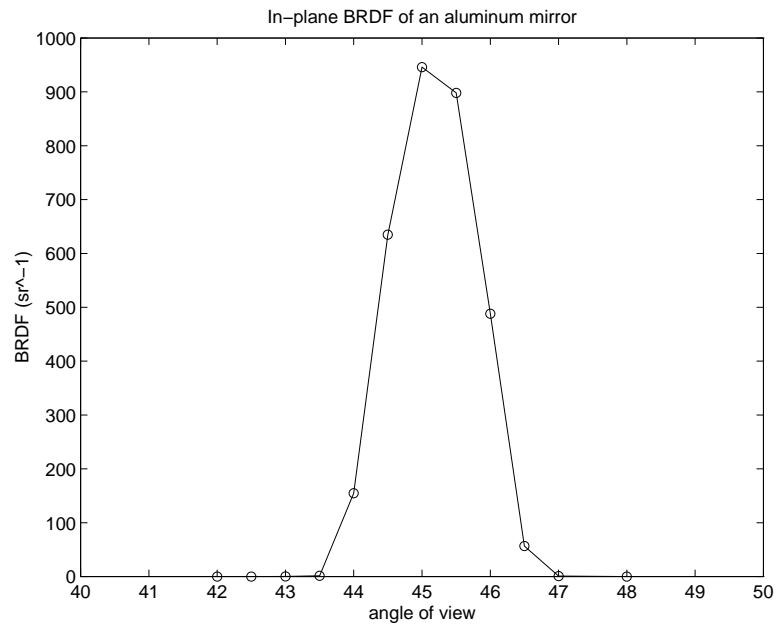


Figure 9.2: Measured BRDF of a vacuum coated aluminum mirror on the incidence plane, at incidence angle of 45° and at wavelength of 550nm. The specular reflection of the mirror is equal to the product of the peak BRDF value, the value of the detector solid angle, and $\cos 45^\circ$

is needed, a polarizer is inserted in front of the Nikkor lens of the source assembly to create a polarized source. The detector also has a polarizer placed in front, and every measurement, regardless of the source's polarizations and detector's polarizer's orientation, is adjusted for the detector's polarization bias.

In making the polarized specular reflection measurement, we have assumed that there is no cross-polarization in the reflection. In other words, we assume that an s polarized light incident on the aluminum and plastic samples will have a reflected light consist only of s polarization, and the same assumption is made for a p polarized incident light.

The measured specular reflections presented in this section are calculated as follows:

1. We use an unpolarized source. The s and p components of the source (measured as $V_{s,direct}$ and $V_{p,direct}$) are measured. The detector views the source directly through a polarizer, oriented for s and p polarization, respectively.
2. The light reflected off the surface is measured at both s and p polarizations.
3. The specular reflections are $\rho_{s,s} = V_{s,reflected}/V_{s,direct}$ and $\rho_{p,p} = V_{p,reflected}/V_{p,direct}$.

Again, we have assumed that $\rho_{s,p}$ and $\rho_{p,s}$ (the cross-polarized reflectance) are approximately zero for the two samples.

Figure 9.3 shows the measured polarized specular reflectance of a vacuum coated (glass substrate) aluminum mirror. The noisy curve between the s and p polarized reflections, is the specular reflection of the same mirror measured with the Optronic

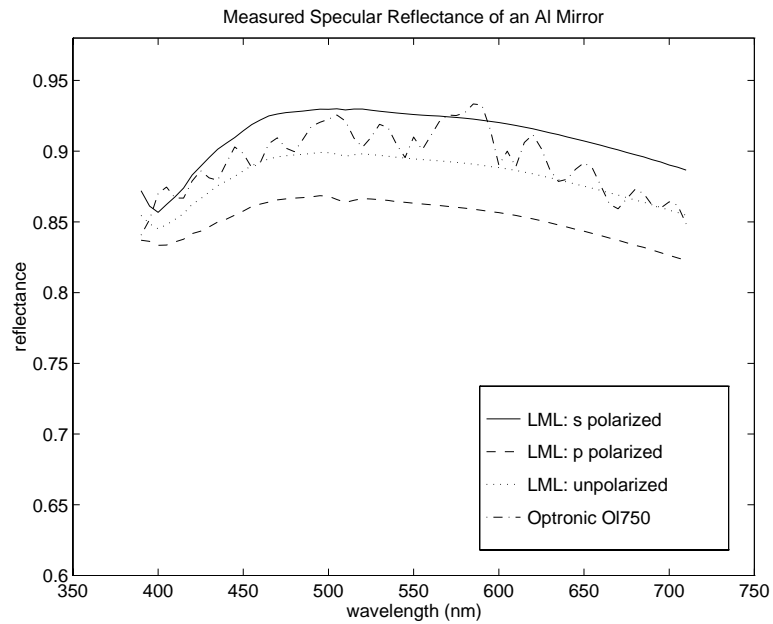


Figure 9.3: Comparison of polarized specular reflectance of a vacuum-coated aluminum mirror at an incidence angle of 45° , measured with the Optronic OL740-75M specular reflectometer and our gonireflectometer. The unpolarized measurement is the average of the s and p measurements. Measurement made by the Optronic OL740-75M has not been adjusted for polarization bias.

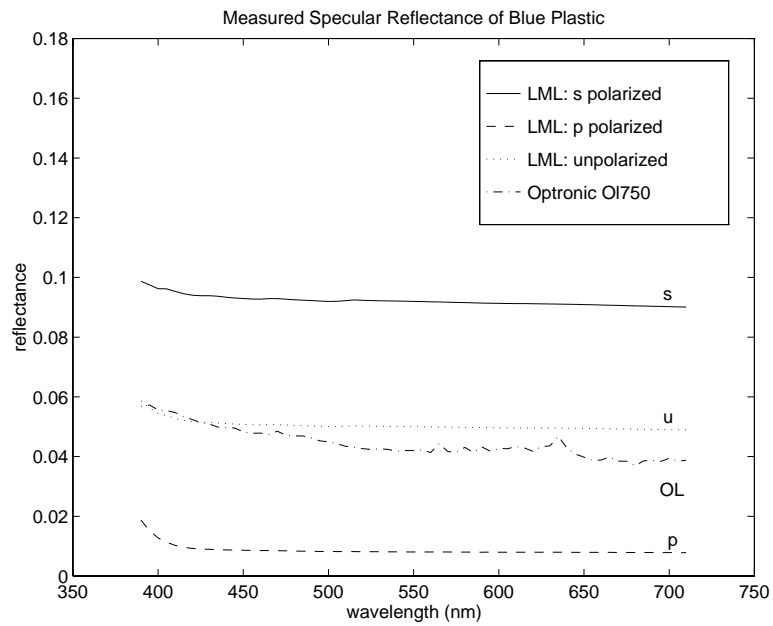


Figure 9.4: Comparison of polarized specular reflection of a blue plastic at an incidence angle of 45° , measured with the Optronic OL740-75M specular reflectometer and our gonireflectometer. The measurement made by the Optronic OL740-75M has not been adjusted for polarization bias.

Specular Reflectometer (OL740-75M). Although the OL750 is a precise instrument, it does not allow polarized measurement. Its incident source on the sample is partially polarized. The unpolarized reflectance shown in Figure 9.3 is the average of the two polarized (s and p) reflectance.

Similarly, Figure 9.4 shows the measured specular reflection at 45° of a smooth blue plastic lucite. The ratio of s and p measurements for the blue plastic is relatively large, compared to the case of the aluminum, indicating a partial polarization of light. It is not surprising for the reflection of a dielectric material such as the blue plastic to be partially polarized at an incidence angle of 45° . At Brewster angle, the specular reflection will be totally polarized in the s direction.

9.3 Bidirectional Reflectance

In this section, we examine the BRDF's of three different materials:

1. a Spectralon (PTFE) sample from Labsphere
2. a latex blue paint (Pratt & Lambert, Vapex Interior Wall Base I, Color #1243 Cal. III.),
3. a stainless steel plate with matte-finish (Q-Panel R-46²)

The three materials each possess a unique type of scattering behavior. The Spectralon is a highly diffuse (close to Lambertian) material. It is spectrally flat

²The R-46 steel plate is manufactured by Q-Panel Company in Cleveland Ohio. They make various metal plates used as industry standards for metal surface finish.

and is widely used as a reference material. Comparing the measurement of the Spectralon to other published data provides a systematic cross-check for our instrument. The latex blue paint is a material that has a diffuse (blue base color) reflectance component and an off-specular scattering component, which increases at a high incidence angle. We will later present measurements showing this off-specular scattering phenomenon. The matte-finished Q-Panel is a “high dynamic-range” reflectance sample which has a strong forward scattering part but a relatively small diffuse component. Measurements of the three materials represents a preliminary study of the instrument’s capability of measuring a variety of material reflectances.

9.3.1 Spectralon

Spectralon is a hardened PTFE (polytetrafluoroethylene) manufactured by Labsphere Inc. and is a widely used white reference in the field of reflectometry. Its reflectance is very high ($> 98\%$), highly diffuse (close to Lambertian), and spectrally flat.

The sample used in our measurements is 4.5in. \times 4.5in. \times .25in. in dimension. It was sanded on a 240-A grid abrasive paper with distilled water, and then air dried prior to measuring. According to Labsphere, this would restore the original reflectance of the Spectralon, in case the surface of the sample had been contaminated.

Labsphere has provided the spectral directional-hemispherical reflectance for the Spectralon at an 8° incidence angle. We can thus use the Spectralon as a reference in performing the system calibration for our gonireflectometer for converting mea-

sured reflection signal to BRDF value, as discussed in Section 8.1. We call this type of calibration *integration calibration*. An absolute calibration method, discussed in Section 8.2, is also used with our gonioreflectometer.

Figure 9.5 shows our measured BRDF of the Spectralon at $\theta_i = 0^\circ$ and $\theta_r = 45^\circ$. We present BRDFs calculated using both integration calibration and absolute calibration. Very often, measurements below 425nm are dominated by noise, which can magnify or diminish the calculated BRDF value. Thus, we restrict our operational spectral range to between 420nm and 710nm, although the detector output provides measurements in wavelengths between 390nm and 710nm. A measurement published by the Rochester Institute of Technology [10] is also plotted in Figure 9.5 as a comparison. The three measurements agree very closely – to within 5%. Compared to the results gathered at the BRDF round robin [20] shown in Figure 1.2 and discussed in Chapter 1, our measurements match well with RIT’s.

Polarized BRDF measurements for the Spectralon are shown in Figure 9.6 and Figure 9.7. The incident light is *p* polarized in both cases, and the incidence angles are 30° and 60° respectively. The reflection is measured in both the *s* and *p* polarizations. The view direction ranges from $(\theta_r = 84^\circ, \varphi_r = 0^\circ)$ to $(\theta_r = 84^\circ, \varphi_r = 180^\circ)$, with an angular increment of 3° . The “holes” in the curves are regions where the the light source occludes the detector. Near these regions, we can see a trend in the reflectance increasing towards retroreflection. If the sample is perfectly depolarizing, both “ps” and “pp” curves would be identical. The results are very close to those published by Labsphere, plotted on the same figures in “+” and “×.” Measurements made by our gonioreflectometer are plotted in solid and

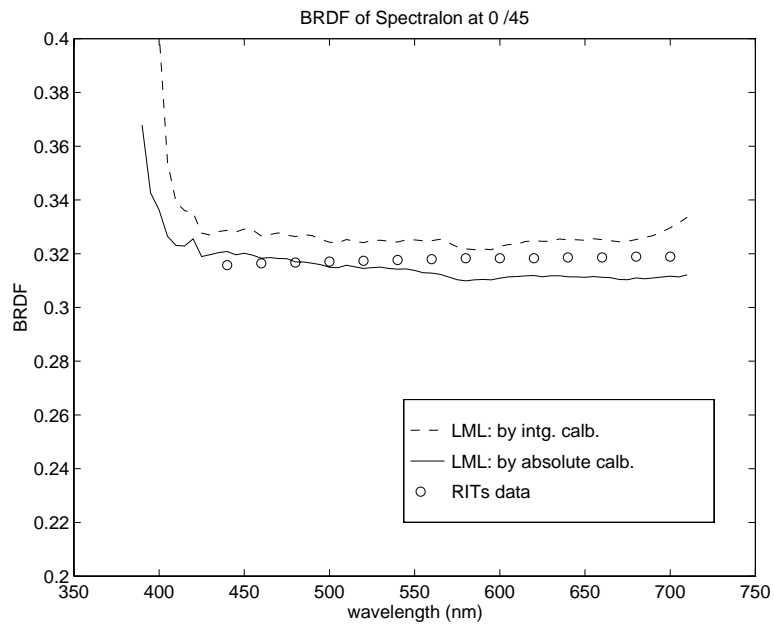


Figure 9.5: Measured BRDF (unpolarized) of Spectralon with source incident at $\theta_r = 0^\circ$, $\varphi_r = 0^\circ$, and view direction at $\theta_r = 45^\circ$, $\varphi_r = 180^\circ$. BRDF calculated by absolute calibration (abs.) and diffuse reference calibration (intg.) are shown. Measured data published by RIT are plotted in circles.

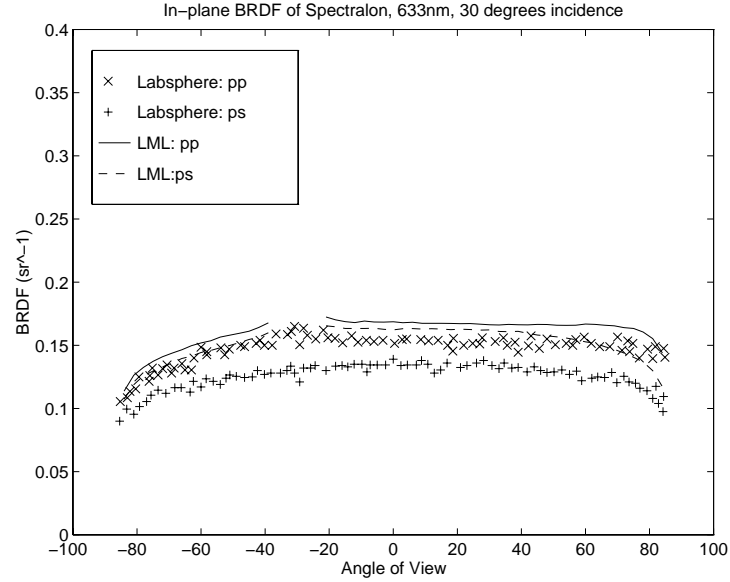


Figure 9.6: BRDF of Spectralon on the incidence plane at $\theta_i = 30^\circ$ for incidence source of p polarization, 633nm wavelength. The reflection is measured for both s and p polarizations. Data published by Labsphere in [27], and measurement made by our gonioreflectometer (LML) are plotted for comparison purposes.

dashed lines and are converted to BRDF values by absolute calibration, as discussed in Chapter 8.2. The discrepancies shown can be attributed to the fact that we are comparing measurements of two different samples with two different instruments, although the Spectralon sample we used was hand-polished according to Labsphere’s recommended procedure. Overall, our measurements show higher reflectance than the data published by Labsphere.

The polarized specular reflectance is measured as follows:

1. The 100% source is first measured at both s and p polarizations with the

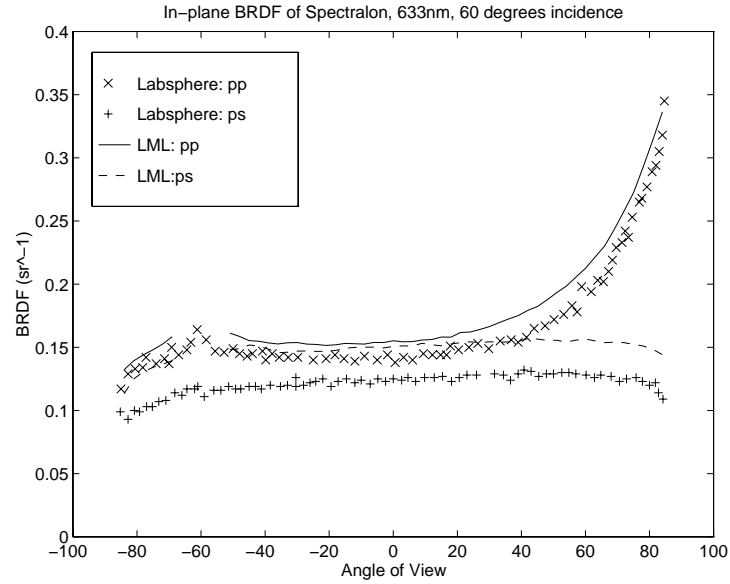


Figure 9.7: BRDF of Spectralon on the incidence plane at $\theta_i = 60^\circ$ for an incidence source of p polarization, 633nm wavelength. The reflection is measured for both s and p polarizations. Data published by Labsphere in [27] and measurements made by our gonireflectometer (LML) are plotted. The measurements agree well.

detector viewing at the source directly. For each of the measurements, the polarizer of the detector is adjusted to match the the source polarization, s and p , respectively. When the source's polarizer and the detector's polarizer are crossed, the detected signal is comparable to the detector's noise.

2. For every polarized incidence on the sample, two polarized reflections are measured.
3. The noise is subtracted from the measurements and the ratio of the incidence and reflected signals is computed.

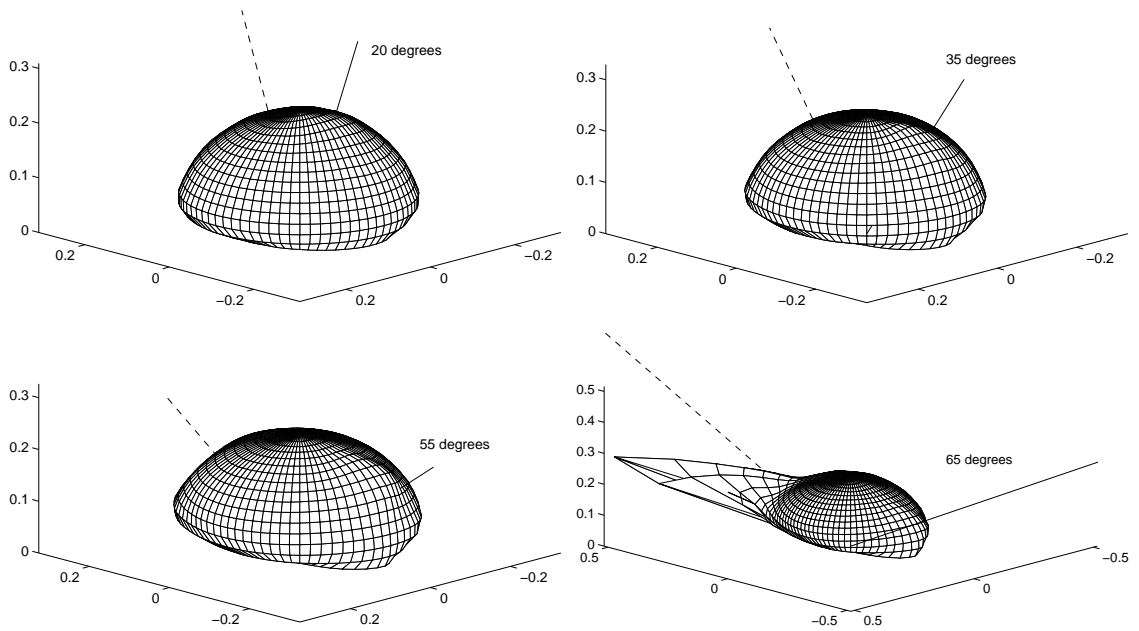


Figure 9.8: BRDF of latex blue paint at a 450nm wavelength at incidence angles of 20° , 35° , 55° , and 65° . The axes are in true BRDF units. The radius from the origin corresponds to the BRDF value. Both the incidence direction (solid line) and the reflection direction (dashed line) lie on the incidence plane.

The details of converting a processed signal to a BRDF value are discussed in Chapter 8.

9.3.2 Blue Paint

Figure 9.8 shows the 3-D plots for the measured BRDF of the latex blue paint over the entire hemisphere above the sample, with incidence angles at 20° , 35° , 55° , and 65° , and a wavelength at 450nm. Similar plots of measured BRDF of the same blue paint with incidence angles at 75° and 85° are shown in Figure 9.9, with

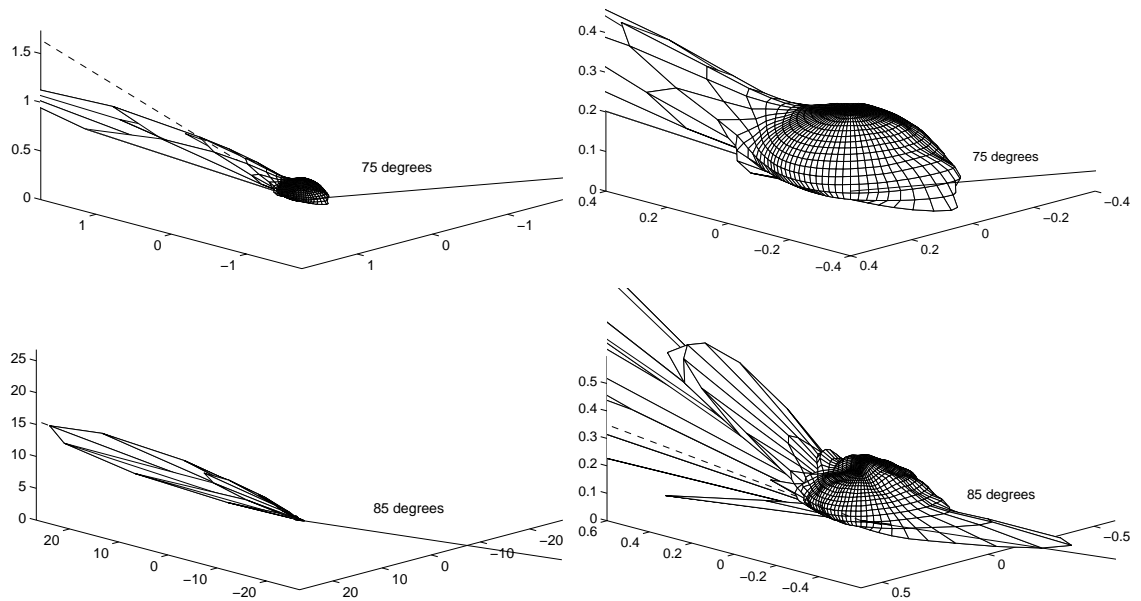


Figure 9.9: BRDF of latex blue paint at a 450nm wavelength, at incidence angles of 75° and 85° . The figures on the right are magnifications of figures on the left. The radius from the origin corresponds to the BRDF value. Both the incidence direction (solid line) and the reflection direction (dashed line) lie on the incidence plane.

accompanying plots at a zoomed in scale. The incidence direction is indicated by a solid line and the specular reflection direction is represented by a dashed line.

Since the actual measurement locations do not lie on a regular polar coordinate grid, to generate the 3D plots in Figure 9.8 and 9.9, we use spline interpolation, first along the latitudes and then along the longitudes. The selection of the original sample locations over the hemisphere is discussed in Chapter 3.5. At $\theta_i = 75^\circ$, the reflection of the blue paint consists of a strong off-specular forward scattering part, and has departed from the close-to-diffuse (Lambertian) shape it has at $\theta_i = 20^\circ$. A significant retroreflection is also observed in the vicinity of the incident direction. The retroreflection shown in the plots was not measured, but was interpolated from the surrounding samples.

As the apparent roughness of the surface decreases toward a high grazing angle, other scattering phenomena arise, as can be seen in the magnified plot on the right column in Figure 9.9 of the 85° incidence.

Figure 9.11 shows the BRDF of the blue paint on the incidence plane for three different incidence angles ($\theta_i = 55^\circ, 65^\circ, 75^\circ$). We can clearly see the increase in forward scattering as the incidence angle increases.

Figure 9.11 and Figure 9.12 are the same reflection curves plotted on different scale. They show the BRDF of the blue paint at $\theta_i = 75^\circ$ on the incidence plane at $\lambda = 450, 550, 650\text{nm}$. As the wavelength increases, the forward reflection increases due to the decrease in the apparent surface roughness. But the diffuse part of the reflection is still dominated by the 450nm wavelength; the color of the blue paint does not change, although the surface becomes more reflective at grazing angles.

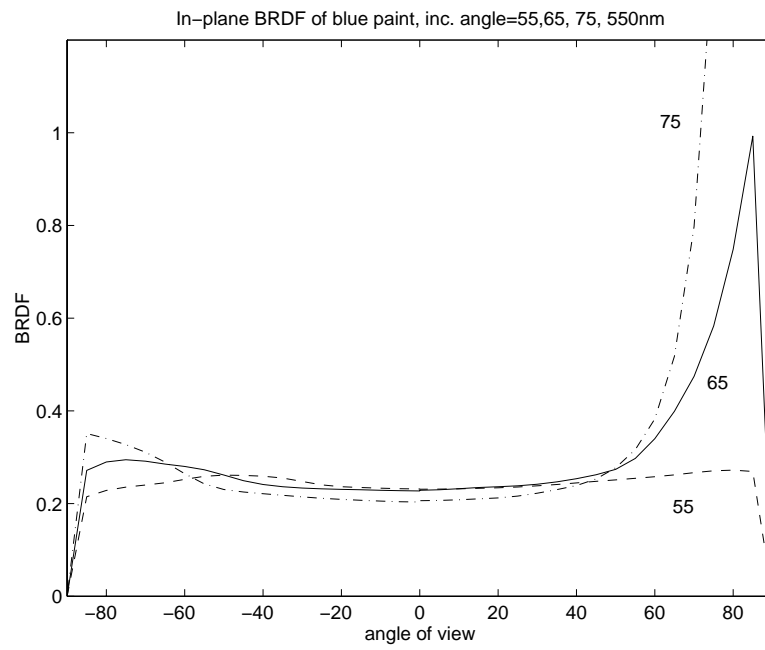


Figure 9.10: Measured BRDF of the latex blue paint at $\theta_i = 55^\circ, 65^\circ, 75^\circ$, on the incidence plane. The forward scattering increases as the incidence angle increases.

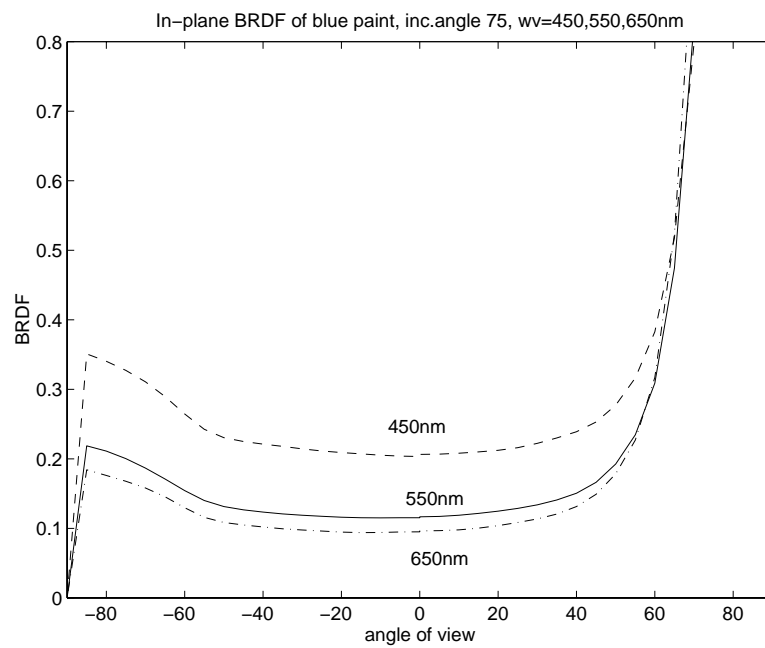


Figure 9.11: Measured BRDF of the blue paint on the incidence plane at $\theta_i = 75^\circ$, and $\lambda = 450, 550, 650\text{nm}$. The forward scattering increases as wavelength increases but the diffuse part is dominated by the “color” of the paint.

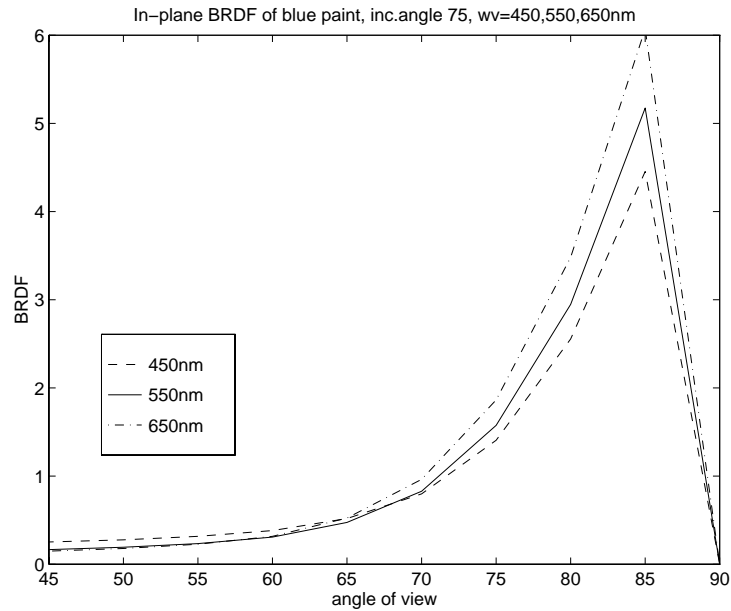


Figure 9.12: These are the same curves as in Figure 9.11 plotted on a larger scale.

9.3.3 Q Panel R-46, Stainless Steel

A point worth noting in measuring samples with BRDFs of high dynamic ranges such as a mirror or the Q-Panel steel plate, is that we need to use the detector at its fastest possible exposure, while still retaining its linear radiometric response. In other words, to increase the signal-to-noise ratio at low light measurement, we need to use as strong a light source as the detector is still able to measure. Both the FXL and ELH lamps are used in our instrument. The FXL has an output of 410W, while the ELH emits at 300W.

Figure 9.13 and Figure 9.14 show the measured BRDF of a steel, matte-finished, Q-Panel (R-46) on the incidence plane, for wavelengths at 650nm and 450nm, respectively. The incidence angle is 60° . As seen from the two figures, the steel plate

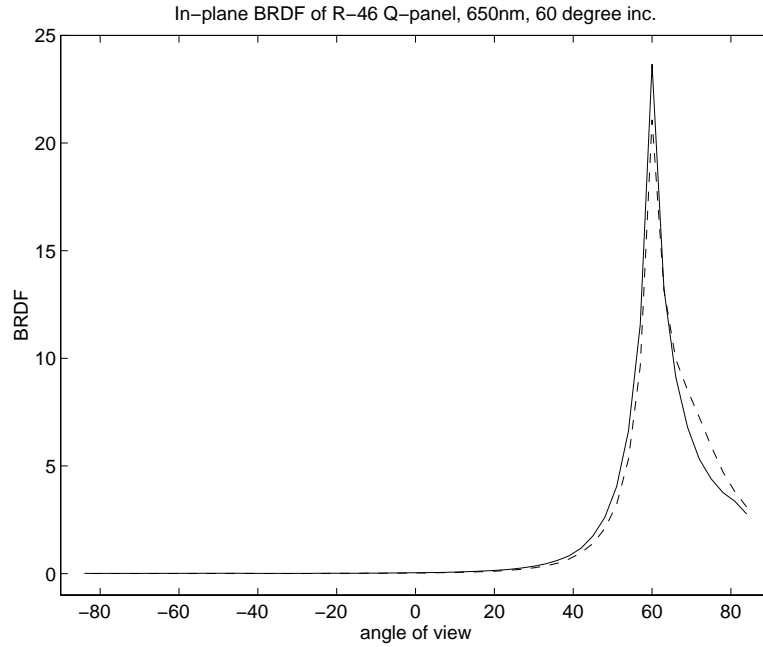


Figure 9.13: BRDF of the Q-Panel R-46, a matte-finished stainless steel, measured in two crossed incidence planes, at $\theta_i = 60^\circ$ and wavelength = 650nm. The two curves are on two crossed incidence planes, one (-) parallel, and the other (- -) perpendicular to the machining direction. The discrepancies indicates the anisotropy of the material.

exhibits strong forward scattering. It does not have a large diffuse component to provide the base color. Unlike the blue paint, the forward scattering of the steel plate does not increase as dramatically as the wavelength increases, or as dramatically as the incidence angle becomes grazing.

9.4 Directional Hemispherical Reflectance

The directional-hemispherical reflectance, ρ_{dh} , for a particular incidence direction, \hat{s}_{i0} , is obtained by integrating the BRDF over the entire hemisphere.

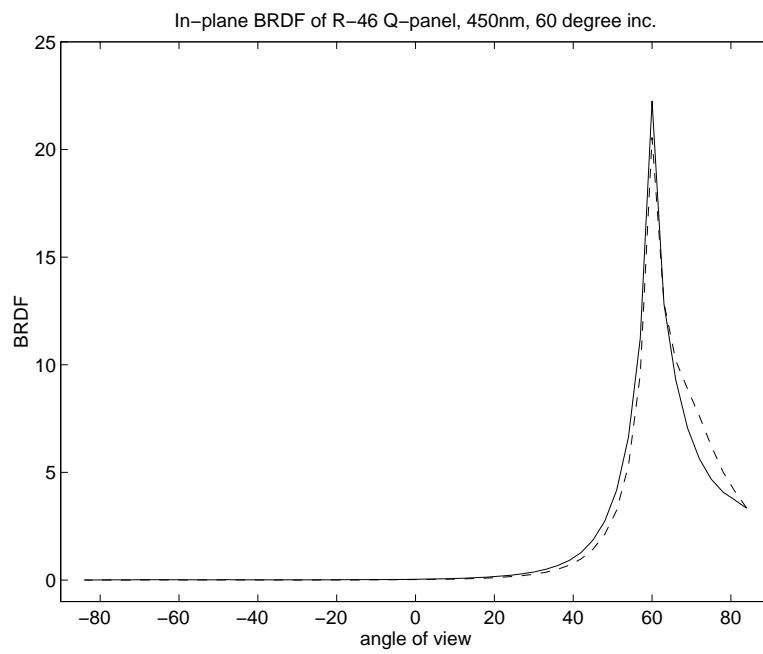


Figure 9.14: BRDF of Q-Panel R-46, a matte-finished stainless steel, measured in two crossed incidence planes at an incidence angle of 60° . The plots are similar to those in Figure 9.13, but with wavelength at 450nm.

$$\rho_{dh}(\hat{s}_{i0}) = \int f_r(\hat{s}_{i0}, \hat{s}_r) \cos \theta_r^i d\Omega_r$$

In this section, we show the variation of the directional-hemispherical reflectance of latex blue paint in both the wavelength and the incidence angle. As an instrument cross-check, we also compare the directional-hemispherical reflectance of the blue paint as calculated from the measured BRDF, with the measurement made by the Optronic OL 740-70 Diffuse-Reflectance Reflectometer.

Figure 9.15 shows the directional-hemispherical reflectance of the latex blue paint as a function of incidence angle at various wavelengths. This figure shows that the albedo increases as the incidence angle increases. Similar data are shown in Figure 9.16. These figures show wavelengths plotted against directional-hemispherical reflectances for various incidence angles. Regardless of the overall increase in the albedo, the reflectance is dominated by wavelengths in 420nm - 520nm for all incidence angles, which indicates the blue color of the paint.

Figure 9.17 shows the comparison between the diffuse reflectance as measured by the Optronic OL740-70 and the diffuse reflectance computed from our measured BRDF. The Optronic OL740-70 uses an integrating sphere to measure the diffuse reflectance. The Optronic measures at an incidence angle of 10° . We present the diffuse reflectance we computed from the BRDF at incidence angles of 0° and 20° . Our computed reflectance came out higher than Optronic's by approximately 7%. The retroreflection component in our BRDF data, interpolated from the data in the vicinity of the retroreflection direction, might contribute to the increase in the

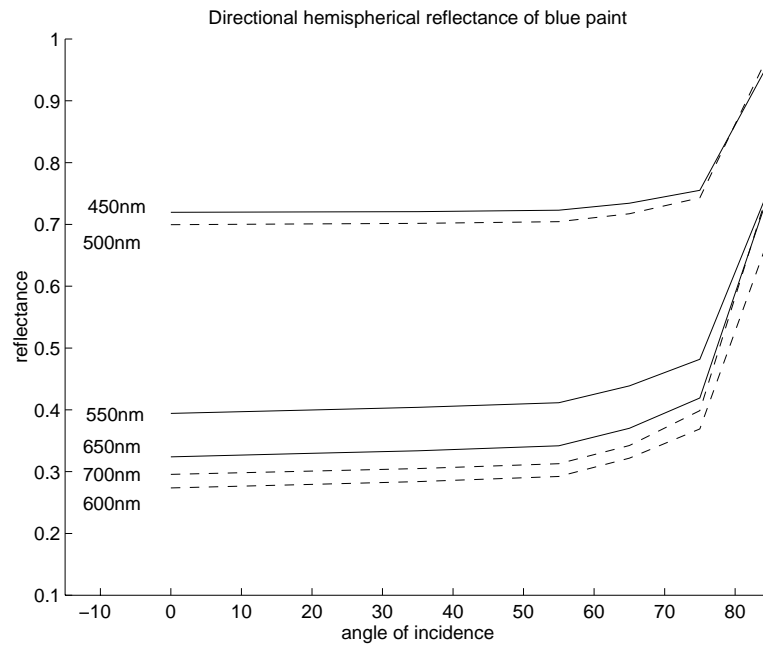


Figure 9.15: Directional-hemispherical reflectance of the latex blue paint, plotted for various wavelengths as a function of incidence angle. The incidence angles where measurements were made are 0° , 20° , 35° , 55° , 65° , 75° , and 85° . The reflectances are computed by integrating the BRDF over the entire hemisphere.

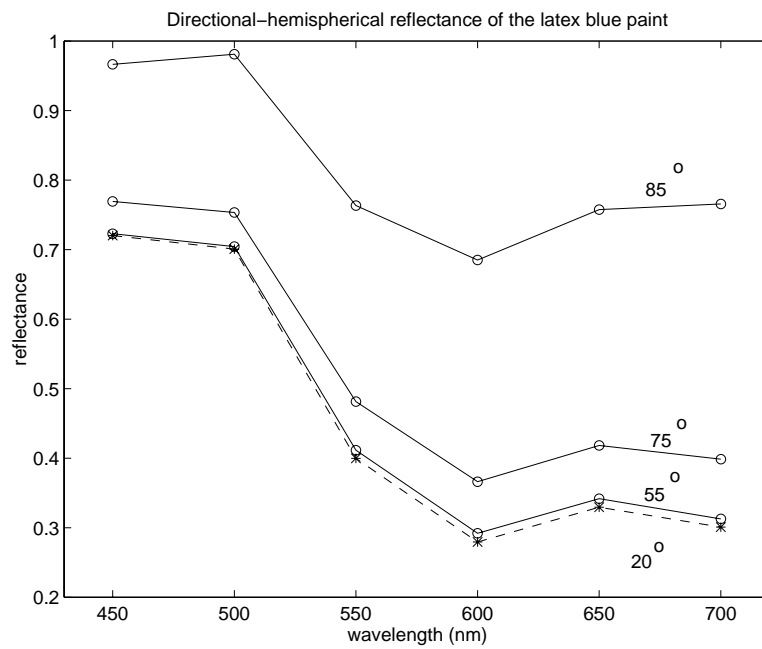


Figure 9.16: Directional-hemispherical reflectance of the latex blue paint as a function of wavelength at incidence angles of 20° , 55° , 75° , and 85° .

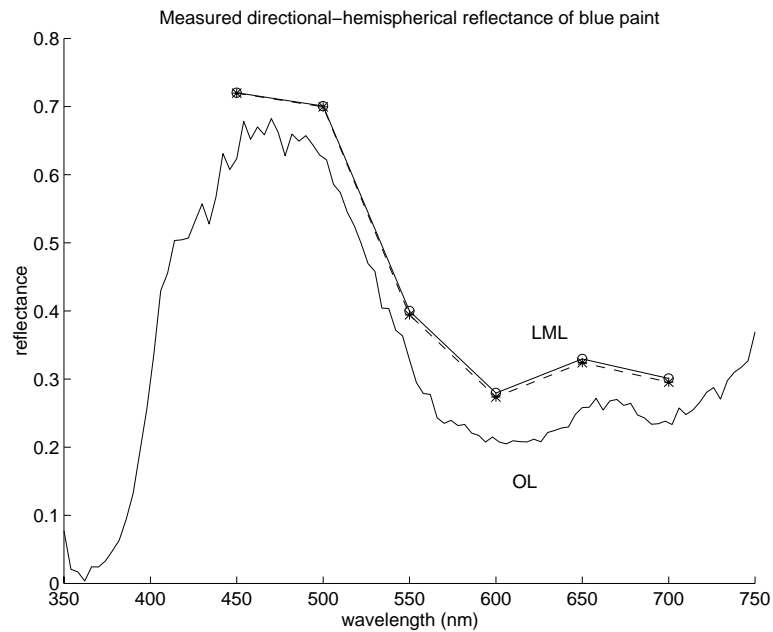


Figure 9.17: Comparison of the directional-hemispherical reflectance of blue paint as measured by our gonireflectometer and by the Optronic OL 740-70. The solid line curve labeled “OL” is the diffuse reflectance of the blue paint as measured by the Optronic OL 740-70 at 10° incidence. The plots labeled “LML” show the diffuse reflectance computed from our measured BRDF. The incidence angles are 0° and 20° for the “- -” and “-” plots, respectively.

integrated directional hemispherical reflectance. If the retroreflection of a sample is relatively high as compared to its diffuse reflection, the retro-reflected light would have escaped the Optronic's reflectance measurement. The variation in reflectance across the paint sample's surface can also account for the discrepancies between the measurements in Figure 9.17.

We also measured the BRDF of the blue paint sample at two different times, where the only condition that was varied was the sample position on the mount. The difference between the directional hemispherical reflectances calculated from these two measurements was 6.6%. We speculate that there is a variation in reflectance across the sample surface which might be caused by the uneven surface roughness – assuming that the paint material itself is perfectly isotropic.

The measurement results presented in this chapter compare favorably with data published by other facilities and measurements made with other instruments. Our gonioreflectometer possesses the adequate dynamic range and angular resolution to measure the reflection of a wide variety of materials, from highly diffuse to highly specular.

Chapter 10

Conclusion

10.1 Conclusion

We have presented the design and specifications of a gonireflectometer that was extensively modified from one that was donated by the Imaging Science Division of the Eastman Kodak Company. The automated three-axis gonireflectometer is capable of measuring the BRDF of a material with isotropic surface reflectance. Two methods of measurements are possible: One is an absolute method based on direct viewing of the source radiation to determine the sample illumination; the other is a comparison method in which integrated measured radiances above a reference sample are compared against the known directional-hemispherical reflectance of the reference surface. In one snapshot, the detector is capable of capturing the reflected radiance in wavelengths ranging from 425nm to 710nm, covering essentially the entire visible range. Except for an area in the vicinity of the retroreflection,

the sampling covers the entire hemisphere above the sample's surface. The highest possible grazing angle is 86° . The specifications for our gonioreflectometer are given in Appendix A. The gonioreflectometer is also capable of measuring specular reflectance.

We took BRDF measurements of the Spectralon (PTFE) at 0° incidence and 45° reflection and these compared favorably (to within 5%) to measurements published by the Rochester Institute of Technology. Polarized measurements at 30° and 60° incidence match very closely to data published by Labsphere, the manufacturer of the Spectralon sample. Specular reflectance measurements of a first surface mirror made by our reflectometer also compare favorably to measurements made using the Optronic OL740-75M reflectometers. Further, integrated BRDF measurements are compared to the measured directional-hemispherical reflectance, as measured by the Optronic OL 740-70 Diffuse Reflectance Reflectometer. BRDF measurements of a steel Q-Panel (R-46) and a latex blue paint are also presented.

10.2 Future Work

The gonioreflectometer we have presented is capable of measuring the BRDF of variety of materials at a vast dynamic range. The instrument is also capable of reaching a high grazing angle of 86° . For the precision of its measurements, it is a relatively fast instrument. It has also been used by more than one user!

A drawback of the gonioreflectometer is that it can only measure the full BRDF in all hemispherical directions for isotropic surface. When spanning the hemisphere

above the sample, the azimuth direction of the incident light cannot be held constant; all reflected directions are measured with respect to the incident light instead of their absolute (θ_r, φ_r) direction in the sample's coordinates. However, the system can be further modified to allow measurements of anisotropic material by adding a motor and stage to rotate the sample azimuthally about its normal. A flexible shaft can be used to rotate the fourth (sample) stage. An add-on module to measure retroreflection should be added to the system.

The main source of angular error arises from the stages being unsteady. The sample stage flexes slightly as it is turned upward. This is a hardware problem that can only be corrected with major parts re-fabrication. A higher powered light bulb can increase the signal-to-noise ratio of the gonioreflectometer. Improving the uniformity of the illumination without upsetting the beam collimation is a task that needs to be undertaken.

Last but not least, a tighter security policy is needed to keep itchy hands off the instrument.

Appendix A

Specifications

The specifications of the gonioreflectometer are listed in this appendix. The recommended settings for the instrument are also listed.

Mechanical System

Rotation stage gear ratio	111.11 (θ_1), 111.11 (θ_2), 80 (θ_3) [steps/ $^\circ$]
Angular accuracy	0.34 $^\circ$
Angular precision	0.01 $^\circ$ (θ_1), 0.01 $^\circ$ (θ_2), 0.013 $^\circ$ (θ_3)

Illumination Source

Light source solid angle, $\Delta\Omega_s$	N/A
Source power drift/stability	0.03% + 5mA
Source spectral stability (over 8 hr.s)	4.5%
Uniformity of source beam	90% (center region), 60% (entire beam)

Test Sample

Sample size	4.5in × 4.5in × .25in
Illuminated area on sample	2.56in. (6.5cm) dia.
Reflecting are on sample	3.08mm × 22mm

Detector System

Detector solid angle, $\Delta\Omega_d$	0.00128sr
Signal readout resolution	16 bit
Detector dynamic range	1:22,000
Effective data dynamic range	450,000:1
Max. BRDF at normal incidence	781.25
RMS of noise	6,000 electrons
Electron sensitivity	1,900 photoelectrons/count
Spectral resolution	2.8nm
Useful spectral range	425 - 710nm

Recommended Detector Settings

Scan mode	Single
Trigger	Internal
Exposure	60ms - 20s
Temperature	15°C

Recommended Motor Settings

	Motor 1	Motor 2	Motor 3
Speed	4000	1800	90 [steps/s]
Acceleration	5	6	6
Step Size	F	F	F

Appendix B

Optical Alignment and Sensitivity

B.1 Aligning the Goniometric Stages

A cylindrical red HeNe laser with a $1/e^2$ beam diameter of 0.6mm and a first surface mirror are used to align the gonioreflectometer stages.

The following are the alignment procedures:

Source arm and sample mount

1. Form a height indicator with an optical post mounted on a base with a piece of wire. Use the wire end as the indicator and set it to the height from the optical table to the center of the suspended Stage II. Call this height $H1$.
2. Mount the laser on the source arm. Check that the laser direction is parallel to the rail by using a sliding target. Adjust the laser such that it travels straight along the middle of the source arm at height $H1$.

3. Move the light source arm to $\theta_3 = 90^\circ$. The roller below the arm should be aligned to the center of the hole along a grid line of the optical table. In the control program, set $\theta_3 = 90^\circ$.
4. Adjust the arm mounting such that the laser beam will hit a dot target near one side of the table at $\theta_3 = 0^\circ$ when the source arm is at $\theta_3 = 180^\circ$ and when the positions are reversed with the target at $\theta_3 = 180^\circ$ and the source at $\theta_3 = 0^\circ$. The height of the target should be $H1$.
5. Move laser source to $\theta_3 = 90^\circ$. Fine-adjust Stage II such that the laser targets its center of rotation.
6. Move the “cradle stage”, Stage I, to $\theta_2 \approx 90^\circ$, and the laser source to $\theta_3 = 180^\circ$. Adjust Stage II such that its center of rotation intercepts with the laser beam.
7. Move the laser to $\theta_3 = 90^\circ$. Place a first-surface mirror on the sample mount.
8. Fine-adjust the positions of the sample mount and the mounting of Stage II such that
 - at $\theta_1 = 45^\circ$, $\theta_2 = 0^\circ$, the source beam is reflected to a point target of height $H1$ at $\theta_3 = 0^\circ$ by the edge of the table.
 - at $\theta_1 = 45^\circ$, $\theta_2 = 180^\circ$, the source beam is reflected to a point target of height $H1$ at $\theta_3 = 90^\circ$ by the opposite edge of the table.
 - at $\theta_1 = 135^\circ$, $\theta_2 = 0^\circ$, the source beam is reflected to a point target of height $H1$ at $\theta_3 = 90^\circ$ by the opposite edge of the table.

- at $\theta_1 = 135^\circ$, $\theta_2 = 180^\circ$, the source beam is reflected to a point target of height $H1$ at $\theta_3 = 0^\circ$ by the edge of the table.
- at $\theta_1 = 90^\circ$, $\theta_2 = 0^\circ$, the source beam is reflected in the incidence direction.
- at $\theta_1 = 90^\circ$, $\theta_2 = 180^\circ$, the source beam is reflected in the incidence direction.

Mechanical defects in the instrument do not allow the perfect alignment described above. However, the sample mount and the mounting of Stage II should be aligned as closely as possible to the the specifications listed above.

9. Move the source to $\theta_3 = 180^\circ$ and the sample to $\theta_1 = 135^\circ$. Check that the beam is reflected onto a point target of $H1$ height at the far end of $\theta_3 = 90^\circ$.

Folding mirror and detector

1. Move the laser source to $\theta_3 = 180^\circ$.
2. Adjust the folding mirror such that it makes a 45° angle with the source beam. The source beam should be reflected 90° to travel above the center of the detector rail to the detector.
3. Make sure that the laser beam hits the folding mirror at its center. The mirror is suspended by optical posts.
4. Use a sliding indicator of height $H1$ on the detector rail to check that the reflected beam is traveling in a straight line along the center of the rail. The

beam should always intercepts the point target on the indicator as it is slid along the rail.

5. Adjust the micrometer at the base of the detector such that the beam hits the center of the detector entrance slit. The detector should be at height $H1$.

B.2 Aligning the Light Source and Detector

The previous section describes the alignment procedure for the gonio-stages and the sample mount. When the light source is mounted in the source arm, the source optics have to be aligned. The detector optics are aligned afterwards.

We use a long optical post with a horizontal indicator to find the height of the center of rotation of the stages, i.e. the point where the rotation axes intersect.

The alignment procedures for the light source and the detector are as follow:

1. Move θ_3 (i.e. the source arm) to 90° .
2. The components of the source assembly are mounted onto the far end of the source arm, with their centers all at the same height level ($H1$). For example, we position the light bulb such that the center of the filament is aligned to the same height of the $H1$ indicator. The optical configuration is described in Chapter 5.
3. The aperture stop (of the source assembly, not the lens) is stopped down to minimum. The lens is focused to the shortest distance.

4. Adjust the lens and other optical components such that the beam is focused onto the center of rotation of Stage II. The beam should travel in a straight line along the source arm.
5. Use a sliding indicator to make sure that the beam travels along the source arm at $\theta_3 = 90^\circ$. The beam should always be centered on the target.
6. Move the source arm to $\theta_3 = 90^\circ$. The source beam should be directed onto the center of the folding mirror and reflected onto the center of the detector.
7. Now, we can install the focusing lens for the detector. The lens is placed such that the source beam is focused onto the center of the detector's entrance slit.
8. To finely adjust the detector focusing optics, turn the source arm back to $\theta_3 = 10^\circ$, place a flat diffuse white material (e.g. Spectralon, or a flat piece of paper) on the sample mount and turn the sample to $\theta_1 = 5^\circ, \theta_2 = 0^\circ$. Focus the the sample's bright spot onto the center of the detector entrance slit.
9. We can also place a gobo, centered at the heart of the beam on the source arm near the sample, to create a sharp-edged beam on the sample. It is easier to identify a sharp-edged image that is focused on the detector.
10. To fine-adjust the centering of the image on the detector, move the sample to $\theta_1 = 85^\circ$ and the source to $\theta_3 = 85^\circ$. What the detector sees from a grazing angle is a thin bright light on the sample.
11. Check the optical alignment again with $\theta_2 = 45^\circ$.

Appendix C

Operating Procedures and Precautions

This appendix presents the operating procedures taking BRDF measurements with the gonioreflectometer using the absolute calibration method. The successive mathematical steps necessary to convert the acquired signals to BRDF values will be discussed in Appendix D. The the procedures described here assumes that the gonio stages and optics of the instrument are precisely aligned and the motor controller is already on. The instructions for aligning the instrument are given in Appendix B.

1. Turn the light source power supply on and turn the current and voltage up to $\approx 90\%$ of the maximum setting for the light bulb. For an ELH bulb, we used $I = 2.34\text{A}$, and for an FXL bulb, we used $I = 4.70\text{A}$. The dial on the power supply should be turned very slowly for at least 5 minutes before reaching the desired setting. Refer to the HP 6030A operating manual for detailed

instructions on operating the power supply.

2. Allow the light source to stabilize for at least 30 minutes before taking any measurements.
3. Open the gonioreflectometer control software and proceed to the detector control section to turn the detector on.
4. Check that the default settings of the detector are as follow:
 - Scan mode: Single scan
 - Trigger: Internal
 - Exposure: 3
 - Temperature: 15° C
5. Move the light source to $\theta_3 = 180^\circ$ and the sample stage to $\theta_1 = 0^\circ$ and $\theta_2 = 0^\circ$. The detector should now be looking directly at the light source.
6. Make a few test measurements, then make the 100% irradiation measurements at both v and h settings for the polarizer. Call these signals V_{0v} and V_{0h} respectively.
7. Baffle the detector completely from the source and take a background reading for both v , and h polarizations. Call them bg_{0v} and bg_{0h} respectively. bg_{0v} and bg_{0h} should be almost indistinguishable from each other. The exposure time, $t_0 = 3 \times 20\text{ms}$, is the same for all V_{0v} , V_{0h} , bg_{0v} and bg_{0h} .
8. Very carefully, mount the test sample onto the sample mount.

9. Move the light source and sample to a position where you think the reflection is minimal. Vary the detector exposure to estimate the exposure time necessary to acquire a reflection signal that is significantly above the noise level¹. If low light reflection is the primary goal, this ratio should be set high.
10. Set the polarizer to v .
11. Take a background reading with the baffle blocking the detector. The background reading function under the detector menu in the gonioreflectometer control software will automatically read the the background at various exposures.
12. Proceed to the BRDF measurement section of the control software and load the preset angular positions for θ_1 , θ_2 , and θ_3 .
13. In the control software, name the data file for the preceding v measurement.
14. When the measurements are completed, repeat steps 11 - 13 for h polarization.
15. When all measurements are completed, quit the control program. It is important not to quit by merely closing the window or shutting down the PC. The quit function writes the current settings of the instrument to a file to be read when the program is re-run.
16. Turn the light source off slowly, avoiding a sudden temperature change in the

¹We do not have to worry about high reflection saturating the detector as the exposure time will automatically be lowered and the measurement will be repeated if clipping occurs.

light source. Careful operation of the light source ensures the spectral stability of the light bulb.

Appendix D

Converting Raw Signals to BRDFs

This appendix shows the mathematical steps involved in converting the reflection signals recorded from the detector to BRDF values. The incident light source is unpolarized. The polarization bias of the detector, $D_{vh}(\lambda)$, is predetermined. The detector views an unpolarized source through a polarizer set at v and h . The ratio of these respective signals is the polarization bias of the detector.

1. The unpolarized 100% source irradiance is obtained as follows:

$$V_0(\lambda) = \frac{1}{2} \left\{ \frac{V_{0v}(\lambda) - bg_{0v}(\lambda)}{t_0 \cdot D_{vh}(\lambda)} + \frac{V_{0h}(\lambda) - bg_{0h}(\lambda)}{t_0} \right\}$$

where bg_{0v} and bg_{0h} are the measured background noises.

2. The signal $V_0(\lambda)$, which consist of 1024 values of λ , is convolved with the smoothing filter, $g(\lambda)$, and then decimated to 65 λ s ranging from 390nm to 710nm.

$$V'_0(\lambda) = V_0(\lambda) \otimes g(\lambda)$$

3. For a data set of $n = 1 \dots N$ measurements (either v or d polarization), there is an associated a set of N exposures, t_n . Each n corresponds to a different θ_r and φ_r , and the incident direction is fixed at θ_{i0} and $\varphi_i = 0^\circ$. Two measurements at v and h are processed to obtained an unpolarized reading.

$$V_n(\lambda) = \frac{1}{2} \left\{ \frac{V_{nv}(\lambda) - bg_n(\lambda)}{t_n \cdot D_{vh}(\lambda)} + \frac{V_{nh}(\lambda) - bg_n(\lambda)}{t_n} \right\}$$

where $bg_n = bg_n(t_n)$ is the predicted background noise for and exposure time of t_n associated with the various n signals, and is calculated from a set of background signals taken at exposures = [50, 100, 500, 1000]detector unit. The details are described in Section 6.5.1.

4. Again, we smooth the signals and decimate them.

$$V'_n(\lambda) = V_n(\lambda) \otimes g(\lambda)$$

5. The BRDF value for each n measurement is calculated as follows:

$$fr_n(\lambda) = \frac{V'_n(\lambda)}{V'_0(\lambda) \cos \theta_i \Omega_d}$$

Appendix E

Reciprocity Test

Three sets of measurements are presented in this appendix to show the instrument's capability in making reciprocal measurements. The first two sets of data are extracted from BRDF measurements of a latex blue paint and a matte-finished steel plate (Q-Panel R-46). The third set of data are measurements made with a Spectralon sample at selected locations to verify that the instrument satisfies reciprocity.

Reciprocal Data from Full Measured Data

The data are listed on the next page. The selected measurements for the latex blue paint sample show that the measurements made by the gonioreflectometer satisfy reciprocity. The results for the Q-Panel show that reciprocity is not satisfied. However, the measurement values that we present are very low compared to the peak values. The variation in texture that is comparable to the size of the reflecting area may account for the discrepancies.

Latex Blue Paint Sample

θ_i	φ_i	θ_r	φ_r	BRDF
0°	0°	55°	0°	0.1256
55°	0°	0°	0°	0.1260
20°	0°	75°	0°	0.1238
75°	0°	20°	0°	0.1248
20°	0°	75°	180°	0.1144
75°	0°	20°	180°	0.1161
20°	0°	75°	90°	0.1170
75°	0°	20°	90°	0.1174
20°	0°	75°	-90°	0.1154
75°	0°	20°	-90°	0.1197
35°	0°	75°	180°	0.1272
75°	0°	35°	180°	0.1209
35°	0°	65°	0°	0.1481
65°	0°	35°	0°	0.1431
35°	0°	65°	180°	0.1315
65°	0°	35°	180°	0.1322
35°	0°	55°	-90°	0.1286
55°	0°	35°	-90°	0.1282
35°	0°	65°	-90°	0.1282
65°	0°	35°	-90°	0.1287

Q-Panel R-46 Steel Sample

anisotropic sample

θ_i	φ_i	θ_r	φ_r	BRDF
0°	0°	75°	180°	0.02
55°	0°	0°	180°	0.001
45°	0°	30°	180°	0.78
30°	0°	45°	180°	0.88
75°	0°	60°	180°	1.18
60°	0°	75°	180°	2.13

Spectralon test results

Figure E.1 shows a series of test measurements made to check if the gonioreflectometer satisfy reciprocity. The test sample used was a white Spectralon with highly diffuse reflectance. Each subfigure in Figure E.1 consists of two measurements of reciprocal directions. Each curve shown is multiplied by the cosine of the incidence angle and normalized by the average of the two curves. A perfect reciprocal pair of measurements would have values at 1. The results in Figure E.1 show that when illumination or view directions are closer to the sample surface, the measurements become less reciprocal.

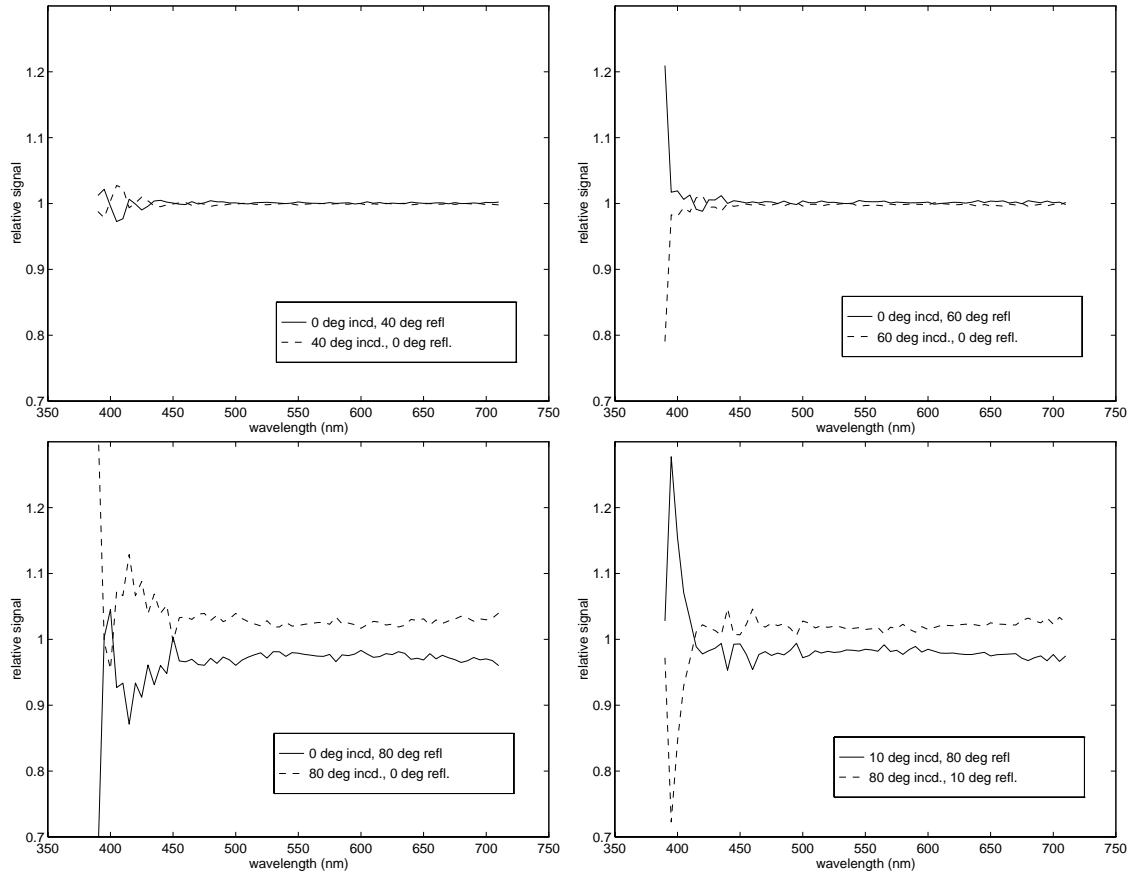


Figure E.1: Reciprocal measurements made of Spectralon sample at various source-view directions. The wavelength is $\lambda = 550\text{nm}$. Each curve is normalized by the average of the two curves. A perfect reciprocal pair of measurements would have values at 1.

Appendix F

Sample Numerical Data

Examples of measured BRDF data on the incidence plane are listed in this appendix.

Spectralon (PTFE) Sample

Sample name: Spectralon

Property: Isotropic sample

Date of Measurement: August 20, 1996

Wavelength = 425nm - 710nm

λ	θ_i	φ_i	θ_r	φ_r	BRDF
430nm	0°	0°	45°	180°	0.330
440nm	0°	0°	45°	180°	0.329
450nm	0°	0°	45°	180°	0.328
460nm	0°	0°	45°	180°	0.328
470nm	0°	0°	45°	180°	0.328
480nm	0°	0°	45°	180°	0.328
490nm	0°	0°	45°	180°	0.328
500nm	0°	0°	45°	180°	0.327
510nm	0°	0°	45°	180°	0.327
520nm	0°	0°	45°	180°	0.327
530nm	0°	0°	45°	180°	0.327
540nm	0°	0°	45°	180°	0.327
550nm	0°	0°	45°	180°	0.327
560nm	0°	0°	45°	180°	0.327
570nm	0°	0°	45°	180°	0.327
580nm	0°	0°	45°	180°	0.328
590nm	0°	0°	45°	180°	0.328
600nm	0°	0°	45°	180°	0.329
610nm	0°	0°	45°	180°	0.329
620nm	0°	0°	45°	180°	0.329
630nm	0°	0°	45°	180°	0.329
640nm	0°	0°	45°	180°	0.329
650nm	0°	0°	45°	180°	0.329
660nm	0°	0°	45°	180°	0.330
670nm	0°	0°	45°	180°	0.330
680nm	0°	0°	45°	180°	0.330
690nm	0°	0°	45°	180°	0.330
700nm	0°	0°	45°	180°	0.330
710nm	0°	0°	45°	180°	0.330

Latex Blue Paint Sample

Sample name: Latex Blue Paint (Pratt & Lambert, Vapex Interior Wall Base I, Color#1243 Cal. III)

Property: Isotropic sample

Date of Measurement: December 1, 1996

Wavelength = 550nm

θ_i	φ_i	θ_r	φ_r	BRDF
35°	0°	5°	180°	0.125
35°	0°	15°	180°	0.127
35°	0°	25°	180°	0.130
35°	0°	35°	180°	0.134
35°	0°	45°	180°	0.139
35°	0°	55°	180°	0.143
35°	0°	65°	180°	0.147
35°	0°	75°	180°	0.152
35°	0°	85°	180°	0.144
35°	0°	5°	0°	0.126
35°	0°	15°	0°	0.129
35°	0°	25°	0°	0.138
35°	0°	45°	0°	0.140
35°	0°	55°	0°	0.132
35°	0°	65°	0°	0.130
35°	0°	75°	0°	0.127
35°	0°	85°	0°	0.114
65°	0°	5°	180°	0.128
65°	0°	15°	180°	0.132
65°	0°	25°	180°	0.139
65°	0°	35°	180°	0.148
65°	0°	45°	180°	0.165
65°	0°	55°	180°	0.204
65°	0°	65°	180°	0.326
65°	0°	75°	180°	0.540
65°	0°	85°	180°	0.999
65°	0°	5°	0°	0.126
65°	0°	15°	0°	0.126
65°	0°	25°	0°	0.128
65°	0°	35°	0°	0.132
65°	0°	45°	0°	0.140
65°	0°	55°	0°	0.158
65°	0°	75°	0°	0.178
65°	0°	85°	0°	0.162

Q-Panel R-46

Sample name: Q-Panel R-46, Matte-Finished Steel Plate

Property: anisotropic sample

Date of Measurement: December 19, 1996

Wavelength = 550nm

θ_i	φ_i	θ_r	φ_r	BRDF
30°	0°	84°	0°	0.008
30°	0°	66°	0°	0.009
30°	0°	54°	0°	0.010
30°	0°	42°	0°	0.014
30°	0°	30°	0°	0.027
30°	0°	18°	0°	0.052
30°	0°	12°	0°	0.075
30°	0°	6°	0°	0.114
30°	0°	0°	0°	0.184
30°	0°	6°	180°	0.303
30°	0°	12°	180°	0.538
30°	0°	18°	180°	1.025
30°	0°	24°	180°	2.203
30°	0°	27°	180°	3.432
30°	0°	30°	180°	3.820
30°	0°	33°	180°	3.273
30°	0°	36°	180°	2.285
30°	0°	39°	180°	1.622
30°	0°	42°	180°	1.186
30°	0°	48°	180°	0.686
30°	0°	54°	180°	0.434
30°	0°	60°	180°	0.296
30°	0°	66°	180°	0.219
30°	0°	72°	180°	0.179
30°	0°	84°	180°	0.126
75°	0°	3°	180°	0.009
75°	0°	9°	180°	0.012
75°	0°	15°	180°	0.018
75°	0°	21°	180°	0.027
75°	0°	27°	180°	0.042
75°	0°	33°	180°	0.066
75°	0°	39°	180°	0.110
75°	0°	45°	180°	0.199
75°	0°	51°	180°	0.374
75°	0°	57°	180°	0.784
75°	0°	60°	180°	1.179
75°	0°	63°	180°	1.837
75°	0°	66°	180°	2.982
75°	0°	69°	180°	5.103
75°	0°	72°	180°	9.073
75°	0°	75°	180°	11.734
75°	0°	84°	180°	9.426

Bibliography

- [1] F.O. Bartell, E.L. Dereniak, and W.L. Wolfe. The theory and measurement of bidirectional reflectance distribution function (BRDF) and bidirectional transmittance distribution function (BTDF). NASA Tech Briefs MFS-28183, March 1979.
- [2] J Blinn. Models of light reflection for computer synthesized pictures. *Computer Graphics*, 11(2), July 1977.
- [3] F.M. Cady, D.R. Bjork, and J.C. Stover. BRDF error analysis. In J. C. Stover, editor, *Scatter from Optical Components*, volume 1165, pages 154–164. SPIE, August 1989.
- [4] F.J.J. Clarke, F.A. Garforth, and D.J. Parry. Goniophotometric and polarization properties of a white reflection standard materials. *Lighting Research and Technology*, 15(3):133–149, 1983.
- [5] R.L. Cook and K.E. Torrance. A reflectance model for computer graphics. *ACM Transactions on Graphics*, 1(1):7–24, January 1982.
- [6] K. Dana, S. Nayar, B. Ginneken, and J.J. Koenderick. Reflectance and texture of real-world surfaces. Technical Report CUCS-048-96, Columbia University, Department of Computer Science, December 1996.
- [7] Commission Internationale de l’Eclairage. Absolute methods for reflection measurements. 1979.
- [8] ASTM Standard E1392-90. Standard practice for angle resolved optical scatter measurements on specular or diffuse surface.
- [9] M. . Fairchild, D.J.O. Daoust, J. Peterson, and R.S. Berns. Absolute reflectance factor calibration for goniospectrophotometry. *Color Research and Applications*, 15(6):311–320, December 1990.

- [10] X. Feng, J.R. Schott, and T. Gallagher. Comparison of methods for generation of absolute reflectance-factor values for bidirectional reflectance-distribution function studies. *Applied Optics*, 32(7):1234–1242, March 1993.
- [11] S.C. Foo and K.E. Torrance. Equipment acquisition for the light measurement laboratory of the cornell program of computer graphics. Technical Report PCG-95-5, Program of Computer Graphics, Cornell University, September 1995.
- [12] D.P. Greenberg, K.E. Torrance, P. Shirley, J. Arvo, J.A. Ferwerda, S. Patanaik, E. Lafortune, B. Walter, S.C. Foo, and B. Trumbore. A framework for realistic image synthesis, To be published in SIGGRAPH 1997.
- [13] X. D. He, K.E. Torrance, F.X. Sillion, and D.P. Greenberg. A comprehensive physical model for light reflection. *Computer Graphics (Proceedings SIGGRAPH)*, 25(4):175–186, July 1991.
- [14] T.H. Himlan. Design of a Light Measurement Laboratory for the Program of Computer Graphics. M.Eng report, School of Mechanical and Aerospace Engineering, Cornell University, August 1987.
- [15] J.J. Hsia and J.C. Richmond. Bidirectional reflectometry. Part I: A high resolution laser bidirectional reflectometer with results on several optical coatings. *Journal of Research of the National Bureau of Standards - A. Physics and Chemistry*, 80A(2):189–205, March-April 76.
- [16] Laurin Publishing Co., Pittsfield, MA. *The Photonics Dictionary*, 42 edition, 1996.
- [17] T.A Leonard. The art of optical scatter measurement. In *High Power Optical Components Conference, Boulder Damage Symposium, to be published by National Institute of Standards and Technology*, 1988.
- [18] T.A Leonard. BRDF round robin. In Breault, editor, *Stray Light and Contamination in Optical System*, volume 967, pages 226–235. SPIE, August 1988.
- [19] T.A Leonard. Listing of optical surface scatter metrology facilities in the united states. TAL92-42, June 1992.
- [20] T.A. Leonard and M. Pantoliano. BRDF round robin. In R. Breault, editor, *Stray Light and Contamination in Optical Systems*, volume 967, pages 226–235. SPIE, August 1988.

- [21] J.C. Martínez-Antón and E. Bernabeu. Automatic three-dimensional spectrogoniometer for determination of optical properties and surface parameters. *Applied Optics*, 34(25):6059–6061, September 1994.
- [22] M.F. Modest. *Radiative Heat Transfer*. McGraw-Hill, New York, 1993.
- [23] F.E. Nicodemus, editor. *Self-study Manual on Optical Radiation Measurements, Technical note 910*, U.S. Department of Commerce, National Bureau of Standards, 1976.
- [24] F.E. Nicodemus, J.C. Richmond, and J.J. Hsia. *Geometric Considerations and Nomenclature for Reflectance*. U.S. Department of Commerce, National Bureau of Standards, March 1977.
- [25] J.C. Richmond and J.J. Hsia. Bidirectional reflectometry. Part II: Bibliography on scattering by reflection from surfaces. *Journal of Research of the National Bureau of Standards - A. Physics and Chemistry*, 80A(2):189–205, March-April 76.
- [26] F.X. Sillion, J.R. Arvo, S.H. Westin, and D.P. Greenberg. A global illumination solution for general reflectance distributions. *Computer Graphics (Proceedings SIGGRAPH)*, 25(4):187–196, July 1991.
- [27] A.W. Springsteen, J. Leland, and T.M. Ricker. A guide to reflectance materials and coatings. Labsphere.
- [28] J.C. Stover. *Optical Scattering: Measurement and Analysis*. SPIE Optical Engineering Press, 2 edition, 1995.
- [29] K.E. Torrance and E.M. Sparrow. Biangular reflectance of an electric non-conductor as a function of wavelength and surface roughness. *Journal of Heat Transfer*, pages 283–292, May 1965.
- [30] K.E. Torrance and E.M. Sparrow. Theory for off-specular reflection from roughened surface. *Journal of the Optical Society of America*, 57(9):1105–1114, September 1967.
- [31] G.J. Ward. Measuring and modeling anisotropic reflection. *Computer Graphics (Proceedings SIGGRAPH)*, 26(2):265–272, July 1992.
- [32] S.H. Westin, J.A. Arvo, and K.E. Torrance. Predicting reflectance functions from complex surfaces. *Computer Graphics (Proceedings SIGGRAPH)*, 26(2):255–264, July 1992.